



**HAL**  
open science

# Loss assessment of the NASA SDT configuration using LES with phase-lagged assumption

Maxime Fiore, Majd Daroukh, Marc Montagnac

► **To cite this version:**

Maxime Fiore, Majd Daroukh, Marc Montagnac. Loss assessment of the NASA SDT configuration using LES with phase-lagged assumption. *Computers and Fluids*, 2021, 234, pp.105256. 10.1016/j.compfluid.2021.105256 . hal-03531474

**HAL Id: hal-03531474**

**<https://hal.science/hal-03531474v1>**

Submitted on 18 Jan 2022

**HAL** is a multi-disciplinary open access archive for the deposit and dissemination of scientific research documents, whether they are published or not. The documents may come from teaching and research institutions in France or abroad, or from public or private research centers.

L'archive ouverte pluridisciplinaire **HAL**, est destinée au dépôt et à la diffusion de documents scientifiques de niveau recherche, publiés ou non, émanant des établissements d'enseignement et de recherche français ou étrangers, des laboratoires publics ou privés.

# Loss assessment of the NASA SDT configuration using LES with phase-lagged assumption (draft)

M. Fiore<sup>a,\*</sup>, M. Daroukh<sup>b</sup> and M. Montagnac<sup>a</sup>

<sup>a</sup>CERFACS, Computational Fluid Dynamics team, Toulouse, France

<sup>b</sup>ONERA, Aerodynamics, Aeroelasticity and Aeroacoustics Department, Châtillon, France

## ARTICLE INFO

### Keywords:

NASA SDT

Large-Eddy Simulation (LES)

Phase-lagged assumption

Proper Orthogonal Decomposition (POD)

Loss assessment

## ABSTRACT

This paper presents the numerical study of the Source Diagnostic Test fan rig of the NASA Glenn (NASA SDT). Large-Eddy Simulations (LES) based on a finite volume approach are performed for the three different Outlet Guide Vane (OGV) geometries (baseline, low-count and low-noise) and three rotational speeds corresponding to approach, cutback and sideline operating conditions respectively. The full stage and nacelle geometries are considered in the numerical simulations, and results are compared to available measurements. The NASA SDT configuration is equipped respectively with 22 fan blades and either 26 or 54 vanes depending on the OGV geometry. The simulation domain could only be reduced to half of the full annulus and would still be a significant cost for the LES. In order to reduce computational cost, an LES with phase-lagged assumption approach is used. This method allows to perform unsteady simulations of multistage turbomachinery configurations including multiple frequency flows with a reduced computational domain composed of one single blade passage for each row. The large data storage required by the phase-lagged approach is handled by a compression method based on a Proper Orthogonal Decomposition replacing the traditional Fourier series decomposition. This compression method improves the signal spectral content especially at high frequency. Based on the numerical simulations, the flow field is described and used to assess the losses generated in the turbofan configuration based on an entropy approach. The results show different flow topologies for the fan depending on the rotational speed with a leading edge shock at high rotational speed. The fan boundary layer contributes strongly to losses with the majority of the losses being generated close to the leading edge for the dissipation due to mean strains and close to the recirculation zone occurring on the suction side for the turbulent kinetic energy production.


## 1. Introduction

Upcoming turbofan architectures known as Ultra-High Bypass Ratio (UHBR) turbofans are oriented towards higher bypass ratio for performance purposes. These architectures, with wide and highly twisted fan blades and a reduced gap with Outlet Guide Vanes (OGVs), induce a rich flow topology that is challenging to describe. The description of losses is also challenging since it requires to capture properly the boundary layer development over the different surfaces, transition processes, wake structures and shock waves close to the tip at high rotational speed. Numerically, this requires the use of high fidelity methods but the high Reynolds number and compressible flow limits the feasibility of such methods. The NASA Source Diagnostic Test (SDT) represents the bypass duct of a modern high bypass ratio configuration and is a good candidate for being studied numerically to have a detailed view of the flow in these configurations. This configuration tested at the NASA John H. Glenn Research Center in 1999-2000 offers a rich experimental database including hot wire measurements [34] and laser Doppler velocimetry [35] in the internal channel for aerodynamics and acoustic duct power levels obtained from a rotating rake [20] which are used for validation. Also, a large number of different numerical approaches have been tested on this configuration from Reynolds Averaged Navier-Stokes (RANS)

approach to unsteady/high fidelity methods. The recent numerical studies of this configuration have been performed for acoustic characterization based on the full annulus configuration. Shur et al. [38] completed a simulation based on Unsteady RANS (URANS) approach for the flow upstream of the fan and Improved Delayed Detached-Eddy Simulation (IDDES) approach [37] in the interstage, OGV, and exhaust regions at approach and sideline operating points for the baseline OGV geometry. Casalino et al. [6] performed simulations based on the Lattice-Boltzmann/Very large LES (VLES) approach using the commercial code EXA PowerFLOW. The influence of inlet turbulence, fan Leading Edge (LE) tripping on the flow around the fan blade were studied and the effect of a liner on the sound radiated was also assessed for the three different OGV geometries at approach operating point.

These studies considering the full annulus are based on different turbulence/near-wall modeling, either by solving the RANS equations in near-wall region or by using a law of the wall treatment. In the current study, the purpose is to simulate the flow in the NASA SDT configuration based on LES [36, 13] without modeling of the near-wall flow region by approaching the requirements for a wall-resolved simulation and minimizing the turbulence modeling due to the sub-grid scale model by a sufficient grid refinement in the simulation domain. For the code used in the study that solves the filtered compressible Navier-Stokes equations, the LES of the full annulus configuration is challenging due to the requirements on mesh quality, numerics, convergence and

\*Corresponding author

 fiore@cerfacs.fr (M. Fiore)

ORCID(s): 0000-0003-1740-4581 (M. Fiore)

## Nomenclature

### Latin letters

$(x, r, \theta)$	cylindrical coordinates	[m]
$(x, y, z)$	cartesian coordinates	[m]
$\dot{m}$	mass flow rate	[kg.s <sup>-1</sup> ]
$\mathcal{V}$	control volume	[m <sup>3</sup> ]
$\mathcal{P}_k$	turbulent kinetic energy production	[kg.m <sup>2</sup> .s <sup>-3</sup> ]
$c$	speed of sound	[m.s <sup>-1</sup> ]
$Re_{C_x}$	Reynolds number based on average conditions at station 1 and midspan fan chord $u_{C_x}/\nu$	[-]
$S$	blade surface	[m <sup>2</sup> ]
$s$	entropy	[kg.m <sup>-1</sup> .s <sup>-2</sup> ]
$C_p$	pressure coefficient	[-]
$c_p$	constant pressure heat capacity	[kg.m <sup>2</sup> .s <sup>-2</sup> .K <sup>-1</sup> ]
$C_f$	friction coefficient	[-]
$C_x$	axial chord-length	[m]
$D$	rotor diameter	[m]
$f$	frequency	[s <sup>-1</sup> ]
$Hi$	shape factor	[-]
$k$	turbulent kinetic energy	[m <sup>2</sup> .s <sup>-2</sup> ]
$L$	length	[m]
$Ma$	Mach number	[-]
$p$	pressure	[kg.m <sup>-1</sup> .s <sup>-1</sup> ]
$q$	heat flux	[kg.m <sup>-2</sup> .s <sup>-2</sup> ]
$r$	radius	[m]
$T$	temperature	[K]
$t$	time	[s]
$u$	velocity	[m.s <sup>-1</sup> ]

### Greek letters

$\delta$	boundary layer thickness	[m]
$\eta$	adiabatic efficiency	[-]
$\gamma$	heat capacity ratio	[-]
$\kappa$	artificial viscosity coefficient	[-]
$\lambda$	thermal conductivity	[kg.m.s <sup>-1</sup> .K <sup>-1</sup> ]
$\mu$	dynamic viscosity	[kg.m <sup>-1</sup> .s <sup>-1</sup> ]
$\nu$	kinematic viscosity	[m <sup>2</sup> .s <sup>-1</sup> ]

$\omega$	rotational speed	[rad.s <sup>-1</sup> ]
$\pi$	compression ratio	[-]
$\Psi$	shock wave parameter	[-]
$\rho$	density	[kg.m <sup>-3</sup> ]
$\theta$	momentum thickness	[m]
$\zeta$	entropy loss coefficient	[-]

### Abbreviations

AP, CB, SL	APproach, CutBack, SideLine
BA, LC, LN	BAse, Low-Count, Low-Noise
BPF	BLade Passing Frequency
LE/TE	Leading Edge/Trailing Edge
LES	Large-Eddy Simulation
OGV	Outlet Guide Vane
POD	Proper Orthogonal Decomposition
PSD	Power Spectral Density
SGS	Sub-Grid Scale model
SS/PS	Suction Side/Pressure Side
TKE	Turbulent Kinetic Energy
URANS	Unsteady Reynolds Averaged Navier-Stokes

### Subscripts and superscripts

$\infty$	upstream condition
'	fluctuating quantity
+	non-dimensional wall-units
$^{\prime-t}$	total-to-total
in/out	inlet/outlet
mean	mean strains
ref	reference
RMS	root mean square
t	total quantity

### Operators

$\langle . \rangle$	statistical averaging operator
$[.]$	Favre averaging operator
$\bar{.}$	LES filtered quantity
$\tilde{.}$	Favre filtered quantity

data extraction. For the purpose of decreasing the computational cost with acceptable resolution, a phase-lagged assumption approach is used. This method assumes that the flow at a fixed time step and any relative position of a fan blade compared to an OGV in the full annulus configuration is described by the relative position of a unique fan blade and OGV at a certain time step. This method allows to reduce the simulation domain to a single passage per row configuration, as proposed by Erdos and Alzner [12]. For the NASA SDT, this approach can be used since the blading geometry is perfectly axisymmetric. The reduction to a single blade passage per row may induce a forcing of the structures similarly to simulation domain with periodic boundary conditions pre-

scribed but makes possible to have a sufficient mesh refinement to use LES. The main difficulty with the phase-lagged approach lies in the necessary storage of the flow variables at each time step over a full passage of the opposite blade at the phase-lagged interfaces. In multi-row simulations, it corresponds to the storage of the flow variables at the interface between rotating (fan stage) and static domains (OGV stage) and on lateral azimuthal conditions. For the meshes and time steps considered in practical turbomachinery simulations, the direct storage represents a significant cost. The most popular method to reduce the data storage cost is to perform a Fourier series decomposition of the temporal signal at the phase-lagged interfaces, as proposed by He [18, 19]. The



**Figure 1:** NASA SDT model installed in the NASA Glenn Wind Tunnel

Fourier series decomposition is truncated to a limited number of harmonics, and the coefficients are updated at each time step with the shape correction method. This method assumes that the flow is perfectly periodic in time, which is a fair assumption in URANS for operating points dominated by periodic rotor-stator interactions (wakes and potential effects). For LES simulation, the periodic assumption is no longer true. In particular, LES includes multiple unknown frequencies, for example non-deterministic small-scale structures in a turbulent wake, for which the characteristic time that needs to be used is unknown. Keeping the limitation of the phase-lagged assumption, a data storage based on a Proper Orthogonal Decomposition (POD) [2] has been developed and implemented in the elsA software [5] by Mouret et al. [29] and is used to perform the present LES simulations. This compression method especially improves some issues associated to the Fourier decomposition and the corresponding spectrum content.

The purpose of this paper is to assess the capability of the LES with phase-lagged assumption and POD data storage to properly capture the physical phenomena in the configuration by comparing against experimental data available: performance quantity and velocity profiles downstream of the fan blade. Then, the approach is used to describe the flow field and the mechanisms of losses in the NASA SDT configuration for the different OGV geometries and operating points based.

The paper is organized as follows: Sec. 2 introduces the configuration and numerical set up; the method proposed to measure the losses generated in the configuration is described in Sec. 3; the comparison of the numerical simulations against the experimental data is presented in Sec. 4; the description of the flow field, including pressure distributions around the blade and near-wall flow, is introduced in Sec. 5; the description of the loss mechanisms is presented in Sec. 6.

## 2. Configuration and numerical methods

The test case used in the study is the NASA/GE SDT conducted at the NASA Glenn Research Center Cleveland,

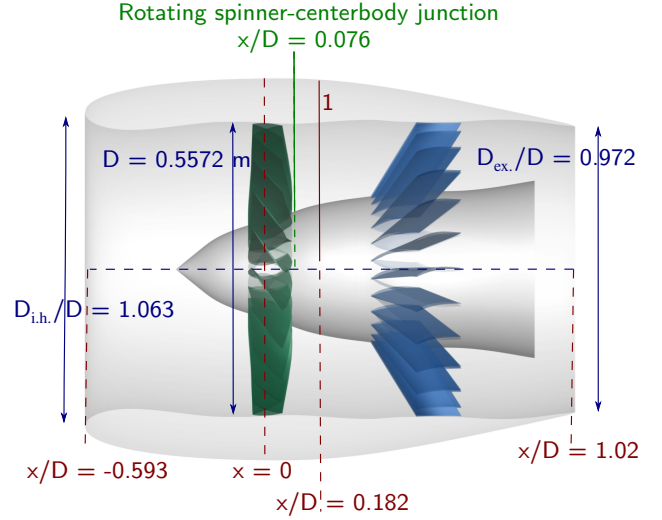


**Figure 2:** Main geometrical features and experimental data measurements location (station 1) for the Low-Noise OGV configuration

Ohio in 1999-2000. The configuration represents the bypass stage portion of a medium pressure ratio, high bypass ratio turbofan engine at approximately 1/5 model scale designed conjointly by NASA and General Electric Aircraft Engines. The NASA SDT configuration has been installed and tested experimentally in a  $2.8 \times 4.6$  m rectangular test section of a continuous flow wind tunnel at atmospheric pressure conditions able to produce velocities up to  $Ma = 0.23$  (see Fig. 1). The configuration shown in Fig. 2 combines a fan with diameter  $D = 0.5572$  m, the OGVs and a flight-type nacelle in an axisymmetric geometry with no core flow. The intake highlight diameter is  $D_{i.h.}/D = 1.063$  and the bypass exhaust diameter is  $D_{ex.}/D = 0.972$ . The origin of the reference system used throughout is located in the midpoint of the fan. The intake lip and bypass exhaust sections are located at  $x/D = -0.593$  and  $x/D = 1.02$  respectively. The location of the junction between the rotating spinner and the centerbody is at  $x/D = 0.076$ . The fan is composed of 22 wide chord blades with a blade tip clearance of  $0.01 C_{x, fan}$  where  $C_{x, fan}$  is the midspan axial fan chord at the design point (100% corrected fan speed). Three different OGV geometries shown in Fig. 3 have been investigated: 54 narrow-chord, high-aspect-ratio vanes representative of a current technology design for this fan pressure ratio (BA); a 26 low-count, wide-chord and low aspect ratio vanes (LC) and a 26 wide-chord, low-aspect-ratio vanes with 30 deg of aft sweep into the vane geometry (LN). Table 1 gathers the main geometrical features of the fan blades and OGVs. Since the purpose of the configuration was to make a fair noise comparison between the three OGV configurations, the total aerodynamic loading for each OGV configuration was kept as equal as possible. This was achieved by keeping the solidity<sup>1</sup> nearly constant. This leads to an airfoil chord grows longer and the gap between vanes

<sup>1</sup>ratio of the vane airfoil chord length to the gap between vanes at a given spanwise location on the vane

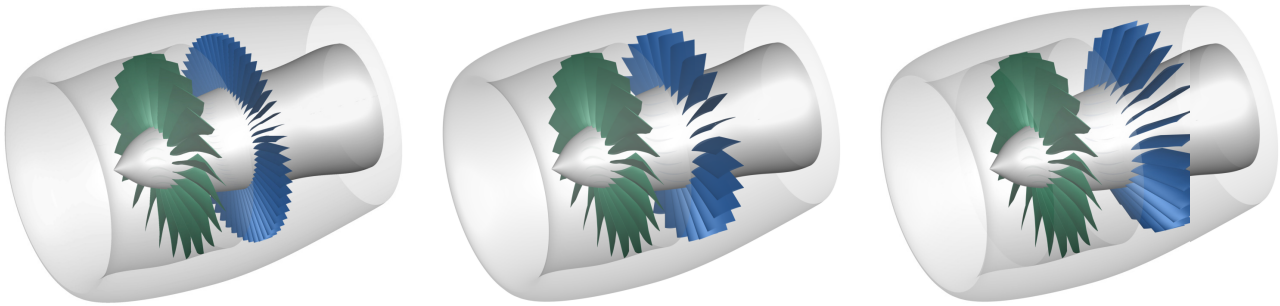


**Figure 3:** Geometrical set up features for the three different OGV designs: BA (left), LC (center), LN (right)

**Table 1**

Geometrical features of the different OGV configurations: BA, LC and LN OGV at pitchline span location

	Fan	BA	LC	LN
No. blades/vanes	22	54	26	26
Stator aft sweep [deg]	-	0	0	30
Axial chord $C_x$ [m]	0.050	0.040	0.082	0.082
Aspect ratio $C_x^2/S$	2.00	3.51	1.67	1.67
Solidity $C_x/\text{pitch}$	1.73	1.52	1.51	1.53
Stagger [deg]	37.10	10.29	10.68	10.75
Vane camber [deg]	-	34.56	37.57	36.06

**Table 2**

Nominal conditions during the experimental campaign for the different operating points

$P_\infty$ [Pa]	101,325
$T_\infty$ [K]	288.15
Incidence angle [deg]	0
Rotational speed $\omega$ [rad.s <sup>-1</sup> ] (% design speed)	AP: 817.6 (61.7%) CB: 1,159.7 (87.5%) SL: 1,325.4 (100%)
$Ma_\infty$	0.1
$Re_{C_{x,\text{fan}}}$ (SL)	$1.1 \times 10^6$

gets larger as the number of vanes is reduced for the LC and LN configurations compared to BA with nearly twice the length of the vane chord, keeping the total airfoil area the same for each configuration.

The engine operates at zero incidence with respect to the engine rotating axis, the Mach number of the wind tunnel is  $Ma_\infty = 0.1$  and the reference pressure and temperature are  $p_\infty = 101,325$  Pa and  $T_\infty = 288.15$  K. Three different operating points are considered: APproach (AP), CutBack (CB) and SideLine (SL). Table 2 gathers the nominal conditions used during the experimental campaign. The simulation domain for the different simulations is shown in Fig. 4. To reproduce the support employed in the experiments, a cylindrical prolongation of the center body has been added to the CAD model provided by NASA. The inlet is set 3 D

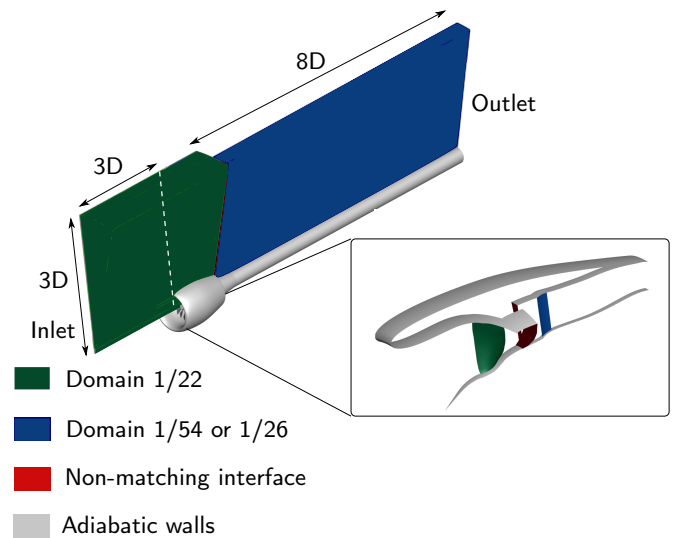


**Figure 4:** Simulation domain. Non-matching interface between rotating and static domains. Domain 1/22-1/54 for the BA operating point, 1/22-1/26 for the LC, LN operating points

upstream of the LE of the nacelle in the streamwise direction. The outlet is set 8 D downstream of the nacelle Trailing Edge (TE) to recover the freestream conditions and prevent reflections at the downstream boundary as the jet exits the domain. The radius of the simulation domain is 3 D. The simulation domain is split in two sub-domains with different azimuthal size: a front domain covering 1/22 of the full annulus domain simulating one of the 22 fan blades and a rear domain covering either 1/54 of the full annulus domain (BA) or 1/26 of the full annulus domain (LC, LN) simulating one OGV. For the internal flow, the interface between the two sub-domains is set between the fan and OGV and on the outer domain at the nacelle TE. At the inlet and on the outer radial surfaces of the computational domain, characteristic boundary conditions with the values of the incoming 1-D Riemann invariants computed by the parameters of the freestream are used without any inlet turbulence injected. At the outlet, the static pressure is set equal to its freestream value, and all the other variables are extrapolated from the interior of the domain (see Tab. 2). Adiabatic, no-slip wall conditions are

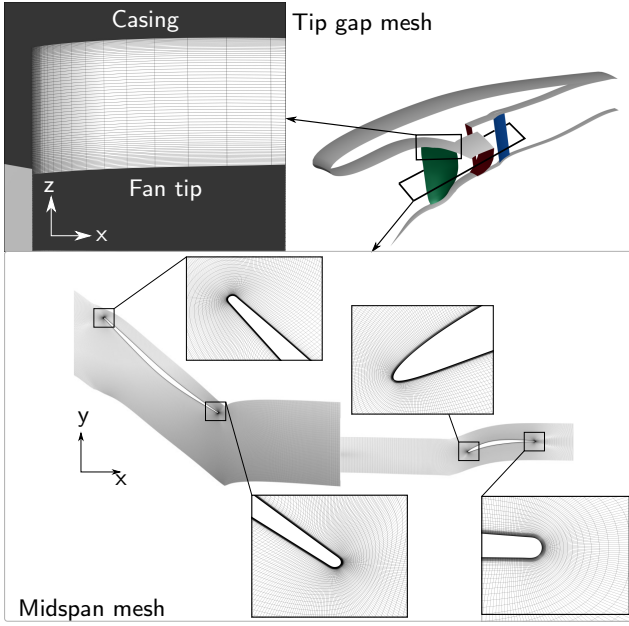
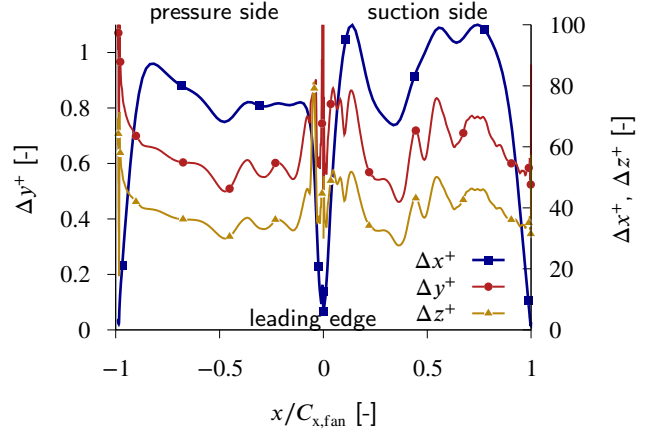


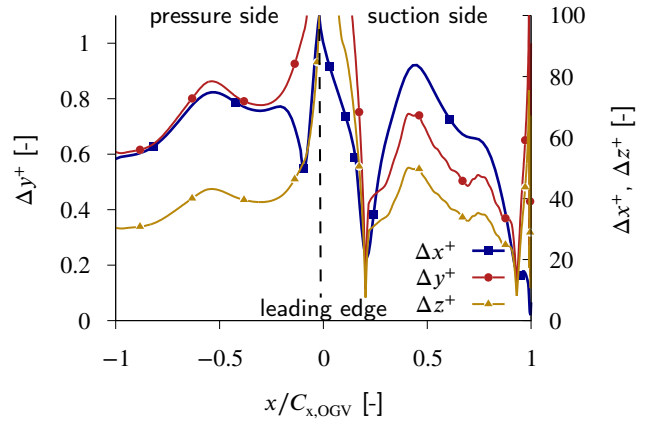
**Figure 5:** Mesh around the fan and BA OGV at midspan and in the fan tip gap

applied on the fan, OGVs, hub, shroud for the internal domain and on the nacelle wall for the external flow. At the non-matching interfaces between the two sub-domains and on the lateral surfaces, phase-lagged conditions are applied.

The mesh structure is based on an O-6H block for the fan and OGV rows. Figure 5 shows the mesh around the fan and BA OGV at midspan and in the fan tip gap. The first off-wall point is set to  $\Delta y/C_{x,\text{fan}} = 4 \times 10^{-5}$ . According to the literature [33, 16, 32], the near-wall region should be resolved with  $50 \leq \Delta x^+ \leq 80$ ;  $\Delta y^+ \leq 1$ ;  $15 \leq \Delta z^+ \leq 25$ . These criteria are challenging to fulfil for the present configuration with relatively high Reynolds number and large dimensions. In wall-resolved LES, it is important to resolve the streaks, i.e., the long and flow aligned structures close to the wall [39]. These structures are shown to have lower variation in the  $x$  direction compared to  $y$  and  $z$  directions. Therefore, the mesh has been mainly coarsened in the  $x$  direction. In the spanwise direction, around 900 layers have been set to reach a spanwise coordinate  $\Delta z^+$  in the range [20,60]. In the streamwise direction, around 300 points have been set to have a streamwise coordinate  $\Delta x^+$  below 100. Figure 6 shows the midspan grid dimensions at the fan and OGV walls (LN) for the SL operating point confirming the targeted value for the first off-wall points. The mesh is built to have an orthogonality higher than 30 deg and in near-wall region higher than 80 deg. The stretching ratio between the size of neighbouring cells in the blade wall-normal direction was set to 1.03 to guaranty around 30 grid points in the viscous layer until  $\Delta y^+ = 50$ . On the spinner, centerbody and casing endwalls, the mesh has been design to have  $\Delta x^+ \leq 100$ ,  $\Delta y^+ \leq 1$  and  $\Delta z^+ \leq 60$ , the stretching ratio between neighbouring cells being set to 1.05. The mesh is refined in the wake to properly propagate the structures developing at the



(a)



(b)

**Figure 6:** Midspan grid dimension at the fan (a) and OGV (LN) wall (b) for the SL operating point

TE of the fan and OGVs. 57 points have been set in fan tip gap. The mesh is composed of around  $210 \times 10^6$  cells for the BA,  $240 \times 10^6$  cells for the LC and LN configurations.

The simulations are performed using the ONERA code elsA [4, 5] which solves the compressible Navier-Stokes equations over multi-block structured grids with a cell-centered approach. In order to speed up the flow development, a RANS followed by URANS with phase-lagged assumption and POD data storage were performed using the LES mesh to get an initial flow field. For the RANS and URANS, an upwind Roe scheme with third-order limiter [31] is used for the convective terms. The Wilcox  $k-\omega$  two-equations model with Zheng's limiter [41] is used for the turbulent transport according to the practice developed by Gourdain [14, 15]. For the RANS simulation, a pseudo-time integration is used to converge towards a steady state. The non-matching interfaces are treated with a mixing plane approach and azimuthal conditions with periodic conditions. For the LES, a second order centred scheme with a low Jameson artificial viscosity [21] ( $\kappa_{\text{jam}}^4 = 0.002$ ) is used for the convective discretization. The subgrid scale model is the Wall-Adapting Local Eddy-viscosity (WALE) [30]. Time integration for

the URANS and LES is performed using Dual Time Stepping with a Crank-Nicholson scheme (second order accurate) in combination with an implicit pseudo-time stepping for the inner loops [26]. The time step is set to a value of  $\Delta t^+ = \Delta t u_\infty / C_{x,\text{fan}} = 3 \times 10^{-4}$  corresponding to 11,880 iterations per full rotation for the BA configuration and 11,440 iterations per full rotation for the LC and LN configurations. The POD compression method relies on successive singular value decompositions of the matrix composed of the conservative quantities at the phase-lagged interfaces stored dynamically during the simulation. At a given time step, the POD modes from the singular value decomposition are sorted in decreasing energy magnitudes and only the first modes are conserved to perform the data compression. For the present study, the 30 most energetic modes are conserved (based on a previous study [29]) and to properly conserve the vortex shedding spectral content generated in the wake of the fan and OGVs at the phase-lagged interfaces. The compressed data stored at the given time step is then imposed later (after a phase-lagged period of time) to the opposite boundary for azimuthal conditions and on the opposed interface for the non-matching interfaces. In addition to the inherent limitations associated with the phase-lag technique described in the introduction, using the phase-lag technique for a single blade passage per row as done in the present study introduces a problem of feedback nature as data is sampled in the same place as it is applied (at the phase-lagged interface). A remedy for this would be to use a three-blade passage per row: the sample data would be extracted in the mid passage azimuthal surfaces and applied on the left and right passages rotational periodic boundaries with a phase lag. The present study is restricted to one blade passage per row due to the large computational cost required but a three-blade passage simulation would be a simple way to ensure that sampling and application is decoupled and thus feedback is avoided. The storage of the flow variables on the phase-lagged interfaces for one full rotation corresponds to a storage requirement of 47.4 GB in POD compared to 155.2 GB for a direct storage. The singular value decompositions performed on the flow field data at each time step at the phase-lagged interfaces to update dynamically the POD coefficients gives a CPU overhead of around 26 % compared to the temporal and spatial integration of the filtered equations in the solver. After the RANS and URANS simulations, 8 full rotations of the configuration have been performed in LES to converge the flow. The mass flow rate in the duct and in the far-field have been checked to be stabilized. Also, first- and second-order statistics have been checked to stabilize by monitoring the signal of probes set in the fan/OGV boundary layers and in the wakes (moving averages until the spectra would stabilize). The three-dimensional temporal averaging used for the comparison against experiments and analysis of the flow field in Sec. 4, 5 and 6 is based on 2860 snapshots equally distributed over two full rotations of the configuration corresponding to 65 snapshots per fan blade passage.

### 3. Measure of loss based on entropy

The increase of entropy denoted  $s$  in the simulation domain is used to describe the loss generated in the configuration as popularized by Denton in a gas turbine context [10]. Entropy increases in the domain due to a viscous and a thermal contribution. The different surfaces of the configuration are modelled with adiabatic walls and no temperature inhomogeneity is imposed in the simulation domain leading to a negligible contribution of the thermal term  $s_{\nabla T}$  and a restriction in the analysis to the viscous term  $s_{\nabla u}$ . In a turbulent flow, the viscous entropy term is divided into a mean term (often called the laminar term) and a turbulent term [23]. The former contribution is only due to the mean flow distortion. The latter contribution is induced by turbulence: the mean flow energy at large scale is dissipated at small scales in internal energy (heat) and induces the non-locality between mean energy flow lost and equivalent heat generated at small scales. In LES, the splitting can be obtained by taking advantage of the unsteady nature of the method. The total viscous irreversibilities  $s_{\nabla u}$  derived in App. A and used in previous studies [27, 40, 23, 22, 9, 24] can be written as:

$$s_{\nabla u} = s_{\nabla u, \text{mean}} + \mathcal{R}_k \quad (1)$$

where  $s_{\nabla u, \text{mean}}$  is the dissipation due to mean strains and  $\mathcal{R}_k$  is the Turbulent Kinetic Energy (TKE) production term. These two contributions can be calculated in each cell grid of the mesh:

$$s_{\nabla u, \text{mean}} = (\mu + \mu_{\text{SGS}}) \left( \frac{\partial [u_i]}{\partial x_j} + \frac{\partial [u_j]}{\partial x_i} \right) \frac{\partial [u_i]}{\partial x_j} \quad (2)$$

$$\mathcal{R}_k = - \left\langle \bar{\rho} u'_i u'_j \right\rangle \frac{\partial [u_i]}{\partial x_j} \quad (3)$$

where  $\mu_{\text{SGS}}$  is the equivalent sub-grid scale viscosity, the overbar  $\bar{\cdot}$  denotes the filtered quantity as an output of the LES simulation. The tilde  $\tilde{\cdot}$  denotes a quantity calculated from the filtered variables  $\bar{\rho}$ ,  $\bar{\rho} u_i$  and  $\bar{p}$ . Thus the calculated velocity is  $\tilde{u}_i = \bar{\rho} u_i / \bar{\rho}$  using Favre filtering. The statistical averaging is denoted by  $\langle \cdot \rangle$  and Favre averaging by  $[\cdot]$  yielding to  $[u_i] = \langle \rho u_i \rangle / \langle \rho \rangle$  for instance. The fluctuating velocity is defined by  $u'_i = \tilde{u}_i - [u_i]$ . Two types of volume integration of these two terms are performed in the study: a volume integration along the spanwise and tangential directions from the inlet of the domain to the position  $x$ :

$$\begin{bmatrix} (s_{\nabla u})_{\text{in} \rightarrow x} \\ (s_{\nabla u, \text{mean}})_{\text{in} \rightarrow x} \\ (\mathcal{R}_k)_{\text{in} \rightarrow x} \end{bmatrix} = \iiint_{\mathcal{V}, \text{in} \rightarrow x} \begin{bmatrix} s_{\nabla u} \\ s_{\nabla u, \text{mean}} \\ \mathcal{R}_k \end{bmatrix} d\mathcal{V}; \quad (4)$$

a volume integration along the spanwise and tangential directions around the position  $x$  of axial length  $dx$ :

$$\begin{bmatrix} (s_{\nabla u})_{x \rightarrow x+dx} \\ (s_{\nabla u, \text{mean}})_{x \rightarrow x+dx} \\ (\mathcal{R}_k)_{x \rightarrow x+dx} \end{bmatrix} = \iiint_{\mathcal{V}, x \rightarrow x+dx} \begin{bmatrix} s_{\nabla u} \\ s_{\nabla u, \text{mean}} \\ \mathcal{R}_k \end{bmatrix} d\mathcal{V}. \quad (5)$$

**Table 3**

Summary of mono-dimensional performance quantity comparison for the different operating points: AP, CB and SL based on the LN OGV

Op. point	$\dot{m}$ [kg.s <sup>-1</sup> ]	$\pi^{t-t}$	$\eta$
Experiments			
AP	26.44	1.153	0.857
CB	37.87	1.343	0.865
SL	43.86	1.483	0.872
RANS			
AP	26.35 (-0.3%)	1.160 (+0.6%)	0.857 (+0.0%)
CB	38.12 (+0.6%)	1.356 (+0.9%)	0.866 (+0.1%)
SL	44.25 (+0.8%)	1.495 (+0.8%)	0.883 (+1.2%)
URANS			
AP	26.40 (-0.2%)	1.159 (+0.5%)	0.863 (+0.7%)
CB	38.05 (+0.5%)	1.360 (+1.2%)	0.87 (+0.5%)
SL	44.05 (+0.4%)	1.50 (+1.1%)	0.882 (+1.1%)
LES			
AP	26.5 (+0.2%)	1.156 (+0.3%)	0.865 (+0.9%)
CB	38.02 (+0.4%)	1.361 (+1.2%)	0.872 (+0.8%)
SL	44.12 (+0.5%)	1.498 (+1.0%)	0.88 (+0.9%)

## 4. Comparison against experimental data

### 4.1. One dimensional performance quantities

In the experiments, far-field inlet conditions (denoted  $\infty$ ) consisting of total pressure and total temperature were measured using a floor mounted rake located upstream of the inlet. These same quantities were determined downstream of the fan at a station denoted 1 (see Fig. 2) using fixed total pressure/total temperature rakes. Each rake consisted of seven radially-distributed measurement sensors from center to shroud casing and each rake was distributed azimuthally. From these measurements the mono-dimensional main flow quantities were calculated: the mass flow rate  $\dot{m}$ , the total-to-total compression rate of the fan  $\pi^{t-t}$  and the adiabatic efficiency  $\eta$  defined as:

$$\pi^{t-t} = \frac{p_{t,1}}{p_{t,\infty}} \quad \eta = \frac{(\pi^{t-t})^{\frac{\gamma-1}{\gamma}} - 1}{(T_{t,1}/T_{t,\infty}) - 1}. \quad (6)$$

The experimental results for the LN OGV configuration at the three different operating points (AP, CB and SL) are compared against the RANS/URANS simulations used to initialize the unsteady calculations and LES with phase-lagged assumption in Tab. 3. The RANS, URANS and LES simulations are in good agreement with the experiments for the mono-dimensional quantities with a largest discrepancy of around 1.2% with the experiments. The increase of the compression ratio and efficiency with the rotational speed is also well predicted. The discrepancy increases with the rotational speed but a fair agreement can be observed. The comparison of the performance quantities against experiments for the BA and LC OGVs showed a similar agreement.

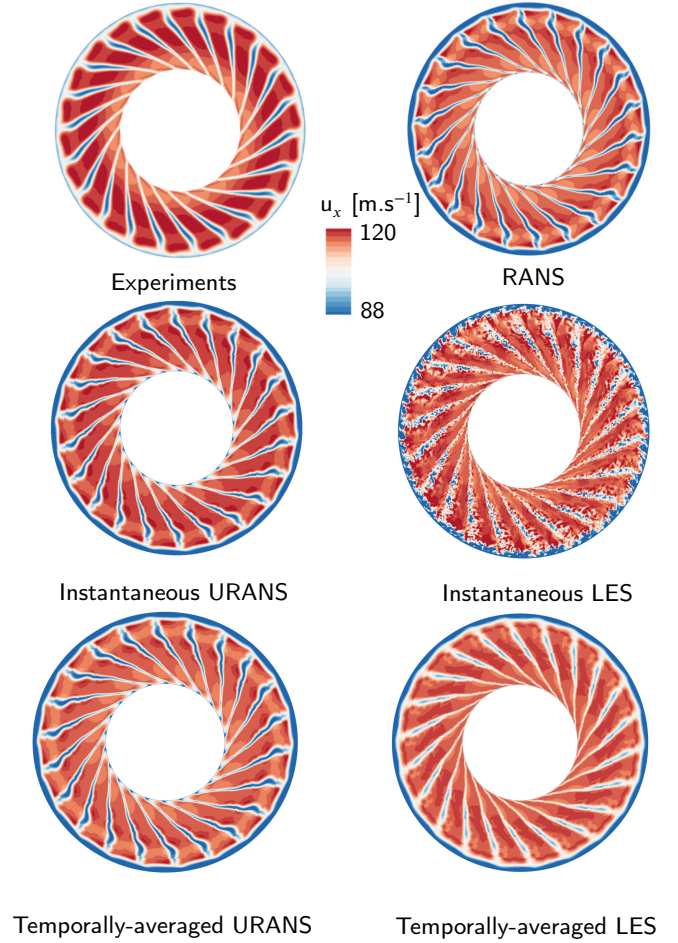
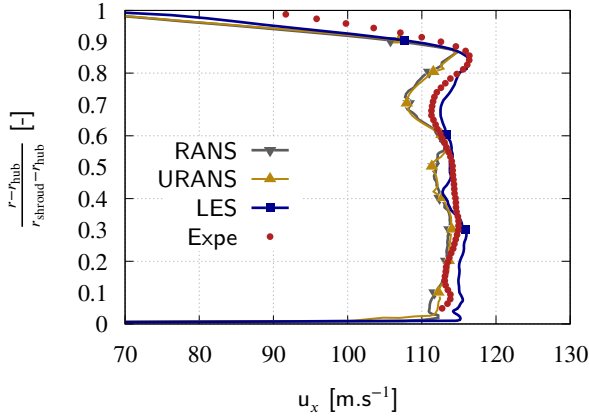


**Figure 7:** Comparison of the axial velocity  $u_x$  at station 1 based on the experiments and numerical simulations

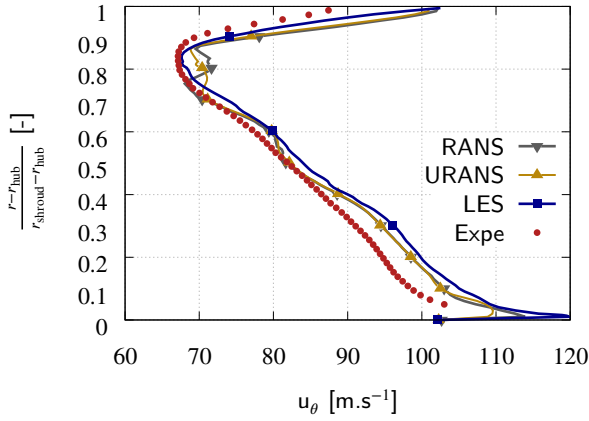
### 4.2. Phase-Locked Velocity Maps

Phase-lock-averaged axial velocity maps  $u_x$  at station 1 for the different numerical approaches and the experiments are shown in Fig. 7. The azimuthal averaging of the 2D map for the axial  $u_x$ , azimuthal  $u_\theta$  and radial  $u_r$  velocities are shown in Fig. 8. The axial, azimuthal and radial velocity profiles are well predicted by the numerical simulation with a maximum discrepancy of 5% compared to the experiments between the hub and 90% of the channel height, the best agreement being achieved by the LES. The main discrepancy occurs within the tip gap where all three velocity components overpredict the velocity break down. The complex turbulent processes occurring in the tip gap flow may be difficult to be predicted even for low level of modeling as in the LES. Figure 9 shows the azimuthally averaged axial  $u_{x,RMS}$ , azimuthal  $u_{\theta,RMS}$  and radial  $u_{r,RMS}$  velocity fluctuations at station 1 for the experiments and LES at AP for the LN configuration. In the tip gap region, the velocity fluctuations are in better agreement compared to the velocity for the three components. The larger discrepancy occurs between 40 and 70% of the channel height. The trend and magni-

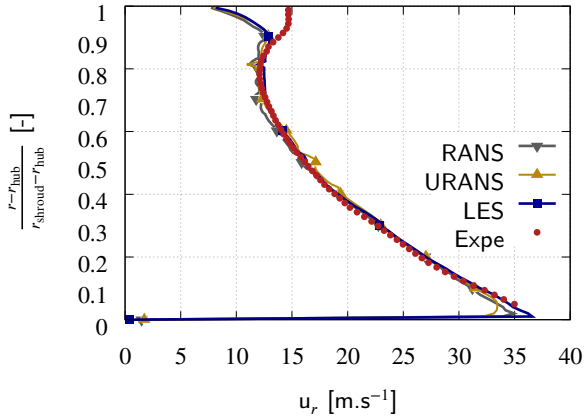




(a)



(b)



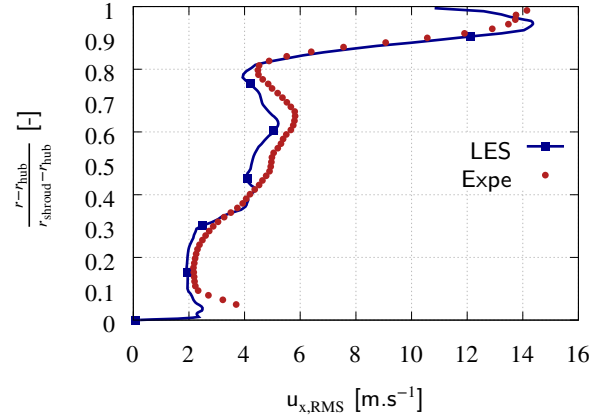
(c)

**Figure 8:** Comparison of azimuthally averaged axial  $u_x$ , azimuthal  $u_\theta$  and radial  $u_r$  velocity profiles at station 1 for the experiments, RANS, URANS and LES at AP for the LN configuration

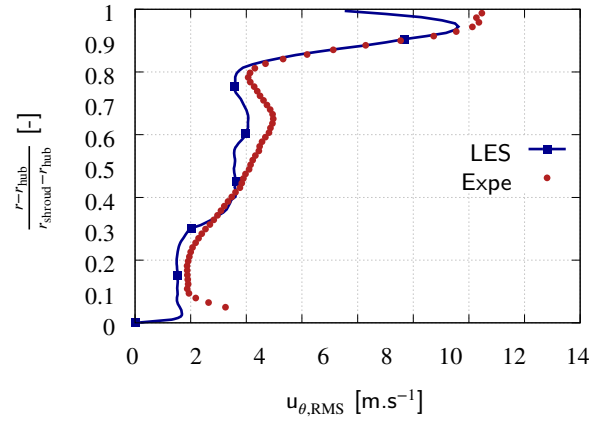
tude of the velocity fluctuations obtained with the LES are however in good agreement with the experiments.

### 4.3. Velocity spectra

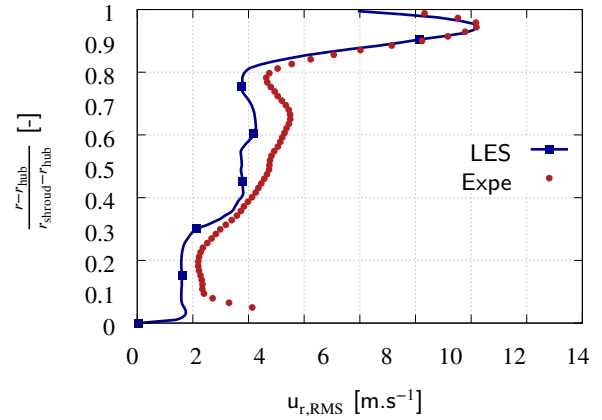
Narrow-band spectra of the velocity fluctuations  $u_{x,RMS}$ , azimuthal  $u_{\theta,RMS}$  and radial  $u_{r,RMS}$  at station 1 at three dif-



(a)



(b)



(c)

**Figure 9:** Comparison of azimuthally averaged axial  $u_{x,RMS}$ , azimuthal  $u_{\theta,RMS}$  and radial  $u_{r,RMS}$  velocity fluctuations at station 1 for the experiments and LES at AP for the LN configuration

ferent channel heights are shown in Fig. 10. The spectra are obtained based on a Power Spectral Density (PSD) of the velocity fluctuation temporal signal at the different fixed radial locations. The PSD is based on a 50% window overlap and Hamming weighting. The radial location extraction corresponds to a position close to the casing ( $r/D = 0.495$ ), 63% channel height ( $r/D = 0.4$ ), 24% channel height ( $r/D = 0.3$ )

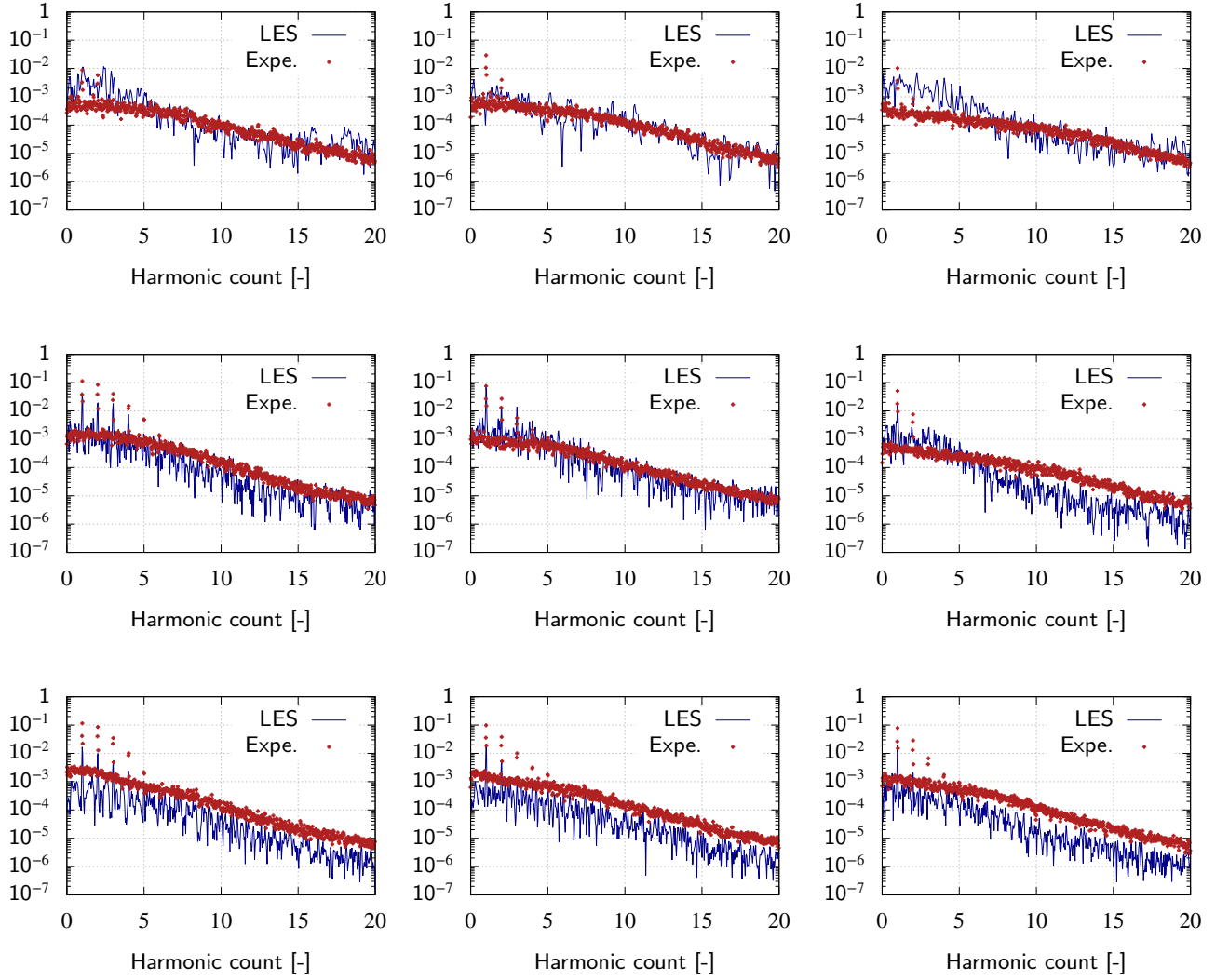


**Figure 10:** Velocity spectra at  $r/D = 0.495$  (top),  $r/D = 0.4$  (middle),  $r/D = 0.3$  (bottom). Axial  $u_{x,RMS}$ , radial  $u_{r,RMS}$ , and azimuthal velocity  $u_{\theta,RMS}$  in the left, middle, and right columns, (in  $m \cdot s^{-1}$ ) hot-wire measurements (symbols) and LES

following the radial position and PSD parameters used by Casalino et al. [6]. However, due to a shorter simulated time in the present study (two full rotations against ten rotations in the study of Casalino et al. [6]) at a sampling frequency of 1430 snapshots per rotation ( $\Delta f = 116,615$  Hz at AP), the frequency bandwidth has been as a consequence extended to 130.13 Hz compared to the 28.6293 Hz frequency bandwidth and produces spectra with more variations compared to this study. The frequency is non dimensionalized by the fan Blade Passing Frequency (BPF) at AP,  $f = 2,862.93$  Hz. Very close to the casing (see Fig. 10 top), the spectra are well predicted in terms of magnitude for all three velocity fluctuations components ( $u_{x,RMS}$ ,  $u_{r,RMS}$ ,  $u_{\theta,RMS}$ ) except a higher level for the axial and azimuthal velocity fluctuations in the lower frequency band beyond 5 BPF. However, some key frequency peaks corresponding to the first fan harmonics are missing at this radius that would suggest insufficient mesh resolution near the casing. At 63% of channel height (see

Fig. 10 middle), the emerging tones corresponding to the multiples of the BPF emerge similarly to the experiments, the levels are well predicted except for the azimuthal fluctuation underestimated between 5 and 15 BPFs. At 24% of the channel height (see Fig. 10 bottom), the tones corresponding to the multiple frequency of the BPF emerge. However, the level at all frequencies and for all velocity fluctuation components are underpredicted. As observed by Casalino et al [6], this may be due to a transition process initiated too late on the fan blade since the spectra were in better agreement with a tripping of the LE. In the present study, since the transition process is not forced, this may explain the discrepancy. Despite these differences, the LES with phase-lagged assumption and POD data storage matches well the experiments and gives more confidence in its use to describe the flow field and quantify the losses generated in the configuration.

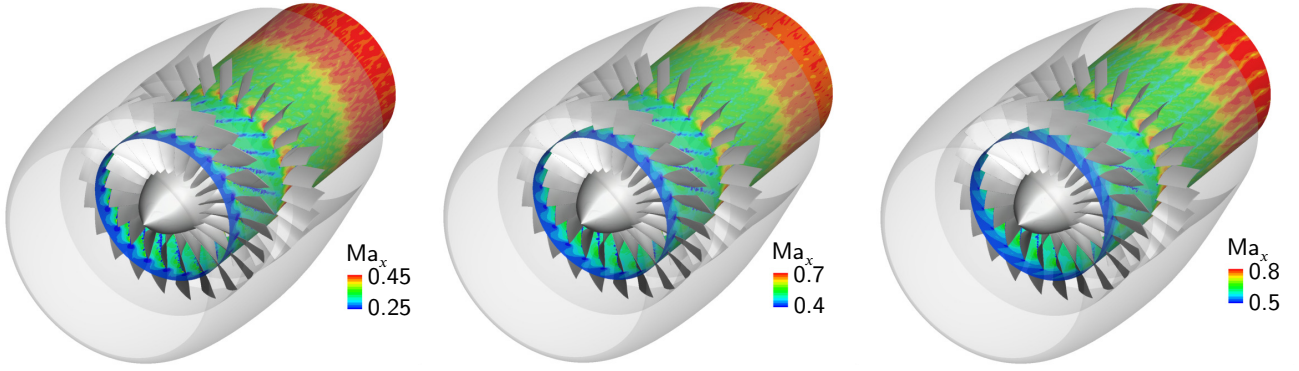


**Figure 11:** View of the instantaneous flow based on a phase-lagged reconstruction colored by the axial  $Ma_x$  at 50% fan span height for the three operating points: AP (left), CB (center), SL (right) and LC configuration

## 5. Analysis of the flow field

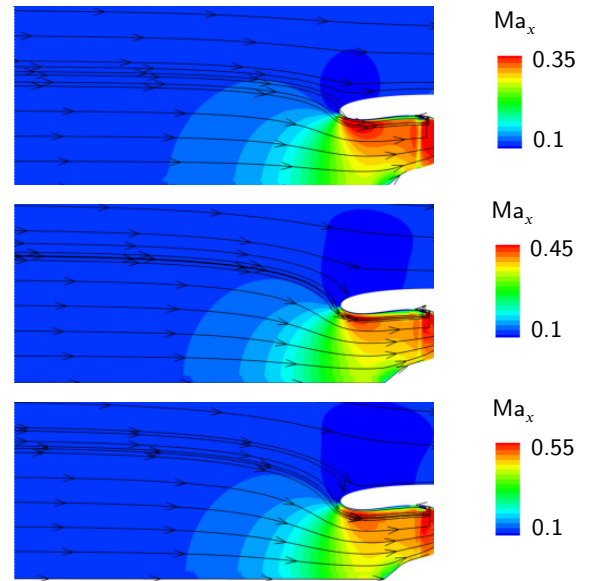
The flow field is first analysed in order to better describe the mechanisms of loss in next Sec. 6. The analysis is based on a temporally averaged solution of the LES simulation used to characterize the flow over the different surfaces of the configuration: pressure distribution, friction coefficient and boundary layer quantities based on the boundary layer edge detection method available in elsA [7, 8]. The boundary layer edge detection method is based on a vorticity criterion similarly to the method proposed by Michelassi et al. [28]: for a considered cell surface, the vorticity is calculated in each cell of the cross section following the structured mesh grid. The minimum and maximum value of vorticity denoted  $\Omega_{\min}$  and  $\Omega_{\max}$  over the cross section are stored. When the value :

$$\Omega_{\text{edge}} = \Omega_{\min} + (\Omega_{\max} - \Omega_{\min}) \times 0.01 \quad (7)$$

is reached by a cell of the cross section starting from the cell at the wall, this mesh point is considered as the edge of the boundary for the considered cell surface point. This procedure is then repeated for any point of the considered surface. The analysis of the flow field is conducted by following the flow through the different components of the NASA SDT configuration for the three different OGV geometries (BA, LC, LN) at the three different operating points (AP, CB and SL). Since the flow field upstream of the OGVs is marginally impacted by the OGV configuration, the description of the flow field upstream of the OGV is made for the LN configuration since the comparison against experiments has been led for this configuration and the flow around the different OGV configurations is then described.

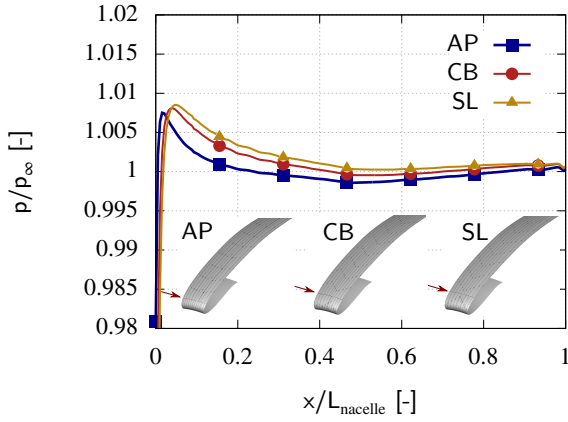
### 5.1. Inlet flow and around the nacelle

Figure 11 shows the instantaneous flow topology at mid fan height for the different operating points. The inlet flow at  $Ma = 0.1$  is progressively accelerated by the fan until  $Ma = 0.35$  at AP,  $Ma = 0.45$  at CB and  $Ma = 0.55$  at SL. Figure 12 shows the axial Mach number and streamlines at the front of the nacelle for the different operating points. The upstream stream tube radius increases with the rotational



**Figure 12:** Axial Mach number and streamlines for the LN configuration at AP (top), CB (middle) and SL (bottom)

speed corresponding to more flow collected through the inlet duct. The increase of the rotational speed induces the stagnation point on the nacelle to be progressively shifted rearward. This behavior can be observed on the pressure distribution around the nacelle shown in Fig. 13 where the maximum pressure corresponding to the rounded front nacelle is shifted with the operating point and based on the streak lines on the nacelle surface. Figure 14 shows the shape factor  $Hi = \delta_1/\theta$  around the external nacelle wall for the AP operating point where  $\delta_1$  and  $\theta$  are the displacement and momentum thickness. These two quantities are obtained locally in each cell surfaces of the configuration by integrating the velocity profile projected on the local streamwise direction at the edge of the boundary and using the local streamwise edge velocity. The boundary layer developing on the external nacelle has a shape factor  $Hi$  close to 2.4. This value characterizes an attached laminar boundary layer until the OGV axial position where the boundary layer separates and reattaches



**Figure 13:** Azimuthally-averaged static pressure evolution along the nacelle wall for the three different operating points

close to the nacelle TE. The boundary layer separation can be observed based on the streaklines having a reversed orientation in the separation region and based on the shape factor around 3.5-4 in this region that generally well characterizes a boundary layer separation. The boundary layer thickness at the TE of the nacelle corresponds to around 1.0% of the nacelle axial length ( $L_{nacelle}$ ) indifferently of the operating point. Figure 15 shows the shape factor and boundary layer thickness over the shroud for the AP operating point. The boundary layer developing from the lip intake on the shroud surface is fully attached and laminar on the convex portion of the intake lip based on the shape factor close to 2.5. When the shroud surface becomes concave (increase of the cross section area), the boundary layer separates forming an enclosed separation bubble characterized by reversed streaklines and a shape factor close to 3.5-4. The boundary layer reattaches causing the transition to a turbulent state of the shroud boundary layer characterized by a shape factor close to 1.3 and a large thickening of the boundary layer. Also, the first vortical structures emerging from the separation bubble and turbulent boundary layer can be observed on the iso  $q$ -criterion (see Fig. 16 left). The boundary layer at the shroud upstream of the fan is very thick corresponding to 6% of the distance between the intake lip ( $x_{lip.in.}$ ) and the fan LE ( $x_{fan}$ ). This behavior of the shroud boundary layer is relatively insensitive of the operating point.

## 5.2. Flow around the fan blade

Figure 18 shows the Suction Side (SS) boundary layer shape factor  $H_i$  and axial friction coefficient  $C_{f,x}$  for the three different operating points. At AP, on the fan SS, the boundary layer separates close to the LE and induces a separation bubble until 10%  $C_{x,fan}$  over all span. This region is characterized by high values of the shape factor (characterizing the separation) and negative axial friction coefficient at the wall induced by the recirculating zone. Figure 19 shows the pressure coefficient distribution around the blade for the different operating points at 10, 50 and 90% of the fan height. The separation bubble is also characterized by a constant

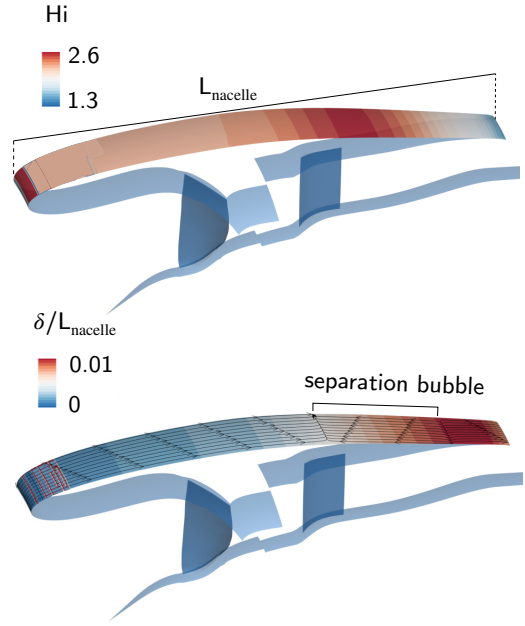


**Figure 14:** Shape factor  $H_i$ , boundary layer thickness and streaklines on the nacelle for the LN and AP operating point

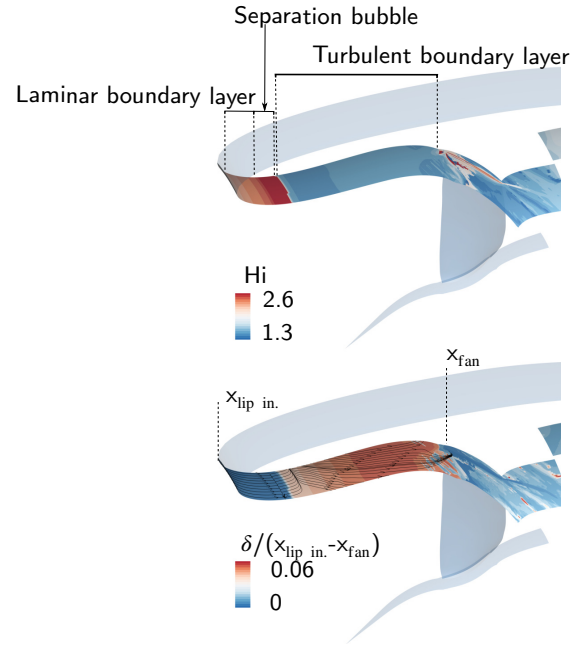


**Figure 15:** Shape factor  $H_i$ , boundary layer thickness and streaklines on the shroud for the LN and AP operating point

value of the pressure coefficient at the different span heights. Based on the LES simulation of the NASA SDT at AP, Arroyo et al. [1] also observed the development of large structures close to the leading edge that can be related to this separation bubble. This separation bubble is induced by a high incidence angle. Indeed, the relatively low rotational speed

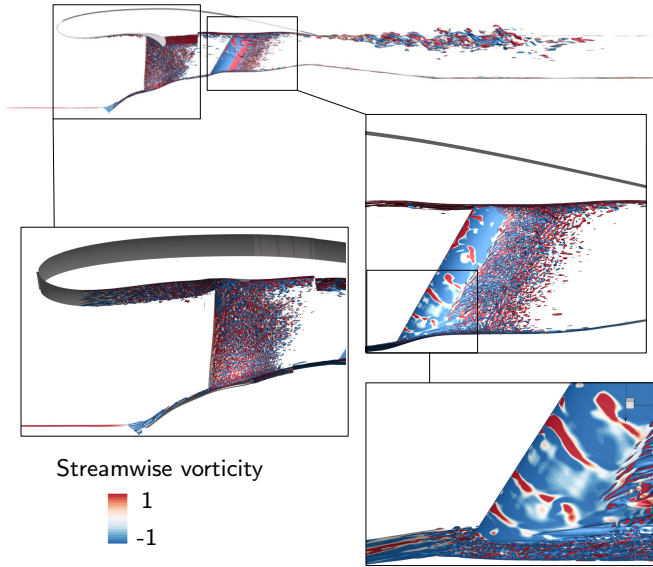


**Figure 16:** Instantaneous view of the fan SS and OGV SS at AP based on a  $Q$ -criterion  $Q = 10^6$  colored by the normalized streamwise vorticity

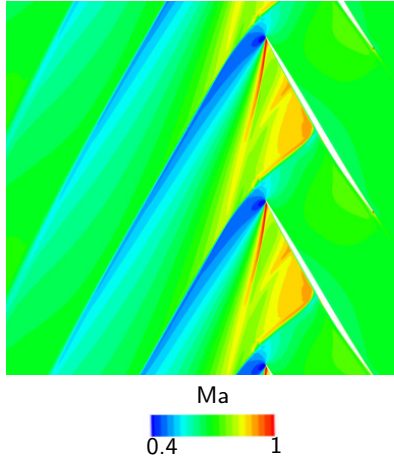


**Figure 17:** Mach contours at 80% fan height for the SL operating point

at AP would result in a decrease of incidence compared to a higher rotational speed at constant mass flow rate. However, since the mass flow rate is reduced at AP (and as a consequence the axial velocity) by more than the rotation speed, the incidence increases and promotes LE separation bubbles. Downstream of the separation bubble, the shape factor decreases until values close to 1.4-1.5 indicating a reattachment of the boundary layer and a transition to a turbulent state. At CB, the near-wall flow behavior is sensibly the same except close to the tip. Figure 17 shows the Mach contours at 80% of the fan height. From 80% span height to the tip, due to the higher rotational speed, a shock wave occurs just upstream of the fan LE. Downstream of the shock, an expansion process occurs and due to the sharp curvature of the fan LE, a region of reacceleration of the flow is induced

characterized by high positive axial friction coefficient delaying the formation of the separation bubble (see Fig. 18 middle). The shock-wave expansion process on the upper part of the blade promotes a large region of constant pressure (see Fig. 19 top). On this upper region of the fan, the transition to a turbulent state is delayed compared to AP. At lower span height, the values of the shape factor are lower compared to AP indicating a more developed turbulent boundary layer. At SL, on the lower part of the fan, similarly to AP and CB, a recirculation zone close to the LE occurs with a constant pressure coefficient (see Fig. 19 bottom). The LE shock wave extends over a larger span height compared to CB between 50 and 100% of the span height due to the higher rotational speed. Similarly to CB, the recirculation zone is delayed further downstream on the fan SS and the transition to turbulent boundary layer is initiated later on the fan SS. Figure 20 shows the boundary layer thickness around the fan SS and PS at midspan for the different operating points. At midspan, the boundary layer thickness at the TE on the SS represent around 10%  $C_{x,\text{fan}}$  for the AP and CB operating points. At SL, the boundary layer thickness at the TE is lower corresponding to 8%  $C_{x,\text{fan}}$  due to the shock-expansion process at the fan LE that delays the development of a turbulent boundary layer.

Figure 21 shows the axial friction coefficient and shape factor on the fan blade Pressure Side (PS) for the different operating points. On the fan PS, the flow is less complex and more two-dimensional compared to the SS. At around 30%  $C_{x,\text{fan}}$  and from midspan to the tip, a region of relatively large shape factor and low axial friction coefficient occurs. However, at AP, the flow remains fully attached and laminar. At CB and more predominantly at SL, the shape factor exceeds 3-3.5 in this region and negative values of the axial friction coefficient are observed characterizing a separation bubble, with a break down in the pressure coefficient at around  $x/C_{x,\text{fan}} = 5\%$ . (see Fig. 19 middle at SL). The boundary layer reattaches downstream and the values of the shape factor close to 1.3 indicate a turbulent boundary layer (see Fig. 21 bottom right). At midspan, the boundary layer thickness at the TE is lower compared to the SS with around 3% of the axial chord at AP and CB and almost 5% of the axial chord at SL.

### 5.3. Flow around the OGV and bypass jet flow

Figure 22 shows the axial friction coefficient and shape factor around the LN OGV for the different operating points. At AP, the SS boundary layer is initially laminar, the streaklines progressively converge and the shape factor is close to 3 at around mid-chord characterizing a separation bubble. The separation bubble can also be observed based on the pressure coefficient at the different span height shown in Fig. 23 with constant values in this region. The boundary layer reattaches and a turbulent boundary layer develops with a shape factor close to 1.3. At CB and SL, the behavior is similar to AP except that the transition is initiated earlier (see Fig. 22 center, right and Fig. 23). Figure 24 shows the boundary layer thickness around the LN OGV SS and PS at midspan for

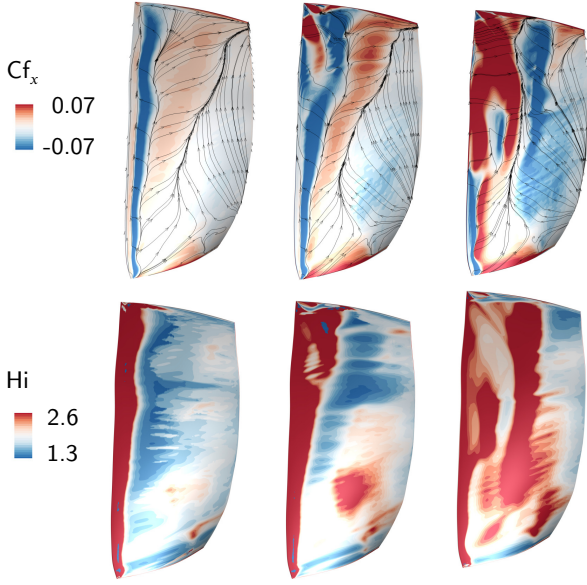


**Figure 18:** Axial friction coefficient  $C_{f_x}$  and shape factor  $Hi$  on the fan SS for the AP (left), CB (center) and SL (right) operating points

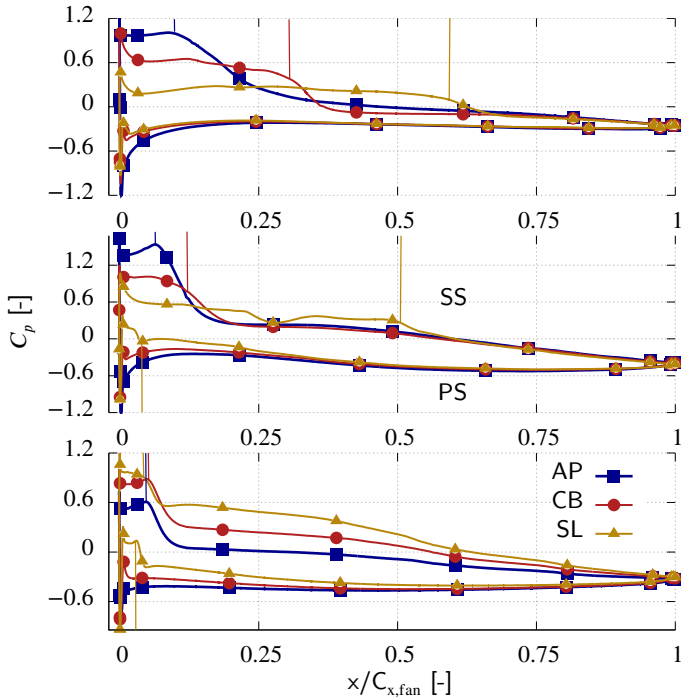


**Figure 19:** Pressure coefficient distribution around the fan at 90 (top), 50 (center) and 10% (bottom) of blade height for the different operating points with the boundary layer transition location (vertical lines)

the different operating points. The boundary layer thickness on the OGV SS represents 7% of the midspan axial chord  $C_{x,OGV}$  at the TE indifferently of the operating point. On the PS, the shape factor is almost constant in span and chord at around 2.5-2.6 characterizing a laminar and fully attached boundary layer with a boundary layer thickness at the TE corresponding to 2%  $C_{x,OGV}$ . Figure 25 show the axial fric-

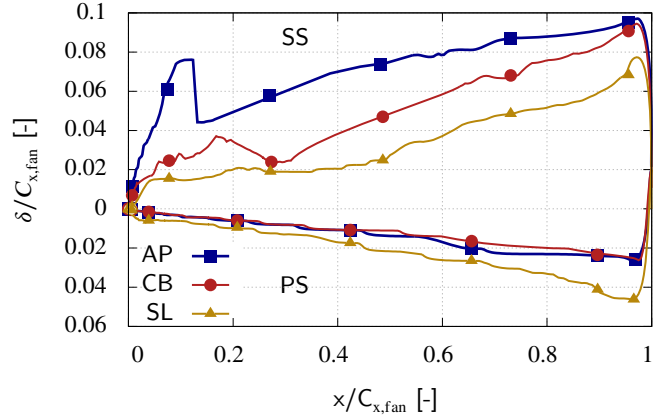


**Figure 20:** Boundary layer thickness around the fan SS and PS at midspan

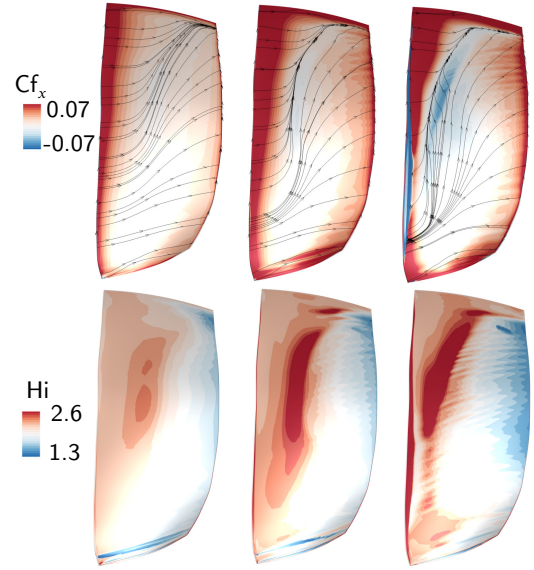


**Figure 21:** Axial friction coefficient  $C_{f_x}$  and shape factor  $Hi$  on the fan PS for the AP (left), CB (center) and SL (right) operating points

tion coefficient and shape factor for the different BA and LC OGV geometries at CB. A similar flow topology is observed for the LC and BA compared to the LN, the separation bubble occurs earlier on the OGV SS for the BA geometry.

Downstream, the flow directed axially by the OGVs is accelerated in the converging nozzle until  $Ma_x = 0.45$  at AP,  $Ma_x = 0.7$  at CB and  $Ma_x = 0.8$  at SL. The bypass flow finally mixes with the flow around the nacelle and generates a shear layer (see Fig. 16 top).

## 6. Loss analysis

The analysis of the losses generated in the configuration is based on the volume integration of the entropy generation rate in each cell introduced in Sec. 3. The entropy loss analysis used here relies on the entropy generation rate to be equal to the sum of dissipation due to mean strains and TKE production corresponding to Eqs.(2-3). This is true if tur-

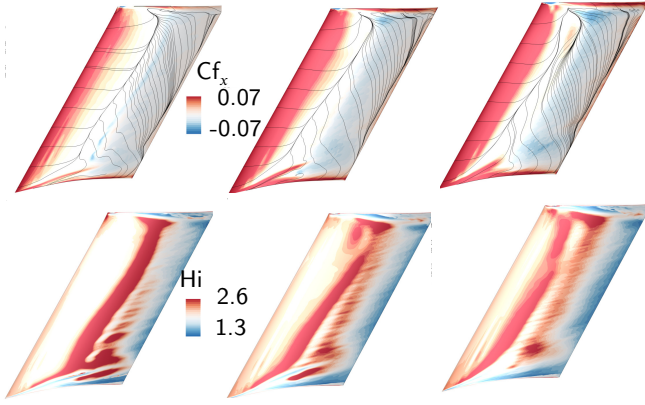


**Figure 22:** Axial friction coefficient  $Cf_x$  and shape factor  $Hi$  on the OGV SS for the AP (left), CB (center) and SL (right) operating points

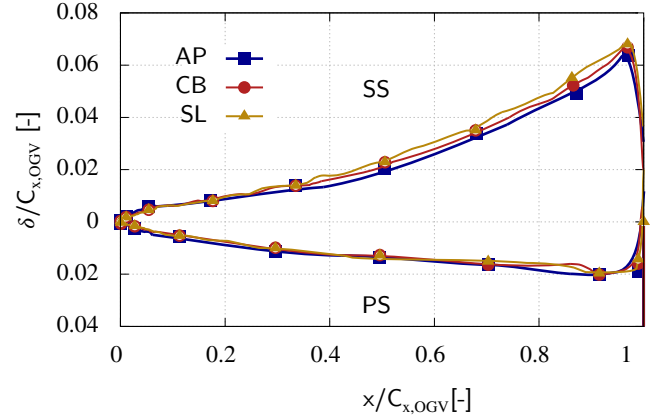


**Figure 24:** Boundary layer thickness around the LN OGV SS and PS at midspan

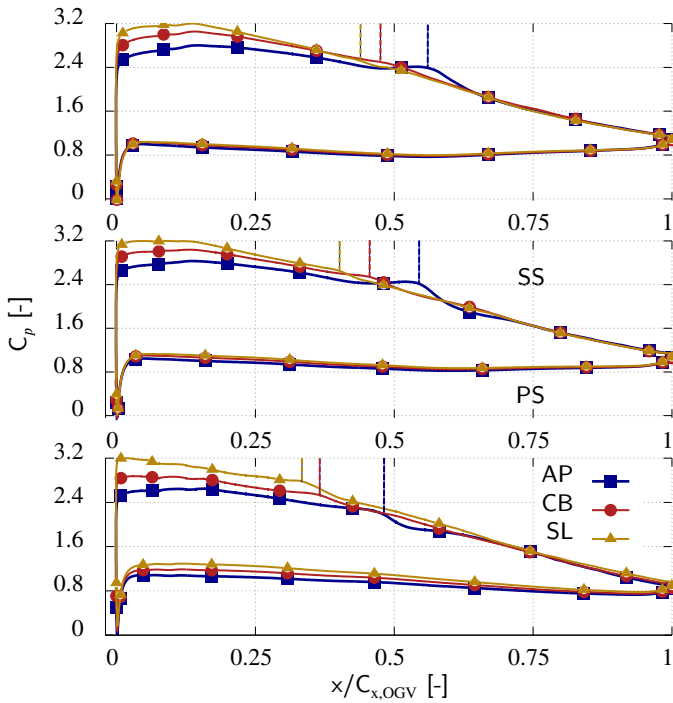


**Figure 23:** Pressure coefficient distribution around the LN OGV at 90 (top), 50 (center) and 10% (bottom) of blade height for the different operating points with the boundary layer transition location (vertical lines)

bulence production is accurately resolved, i.e. the mesh is close to DNS requirements. In LES, a path to compute more rigorously the losses generated consists in quantifying the unresolved part of the turbulence production by considering the modelled Reynolds stresses too (second term in the right hand side of Eq.(18) in App. A). In the present study, only the resolved part of the turbulence production is considered (first term in the right hand side of Eq.(18) in App. A) and due to the relatively coarse mesh, some part of the losses may be hold by the unresolved part of the turbulence production. In order to evaluate the corresponding error, this method to obtain the losses (entropy generation rate) computed in each

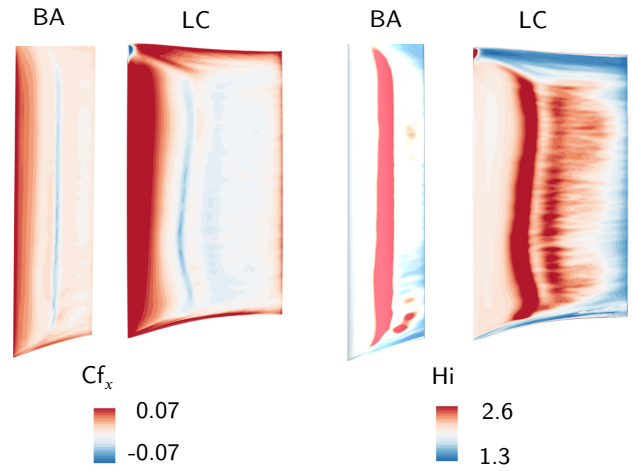


**Figure 25:** Axial friction coefficient  $Cf_x$  and shape factor  $Hi$  on the OGV SS for the BA and LC OGV configurations at CB

grid cell and integrated over a control volume is compared against a second approach to calculate the entropy generated in the simulation domain based on two independent thermodynamic quantities of the flow, for example the pressure  $p$  and temperature  $T$  leading to :

$$s - s_{ref} = c_p \ln(T/T_{ref}) - R \ln(p/p_{ref}) \quad (8)$$

where  $c_p$  is the constant pressure heat capacity,  $R$  the gas constant,  $s_{ref}$ ,  $p_{ref}$  and  $T_{ref}$  reference entropy, pressure and temperature. This method is generally more accurate to evaluate the entropy generated within the simulation domain and is more robust compared to the method used in the present study to evaluate entropy. The volume integral of entropy generation rate led within the whole simulation domain for the CB operating point shows an entropy level 14% lower compared to the method based on the flux of entropy between the inlet and outlet of the domain. The discrepancy between the two methods is non-negligible, the unresolved part of the TKE production can explain partially this discrepancy. Also the estimation of the mean strains dissipation (term function of the filtered velocity squared) and re-

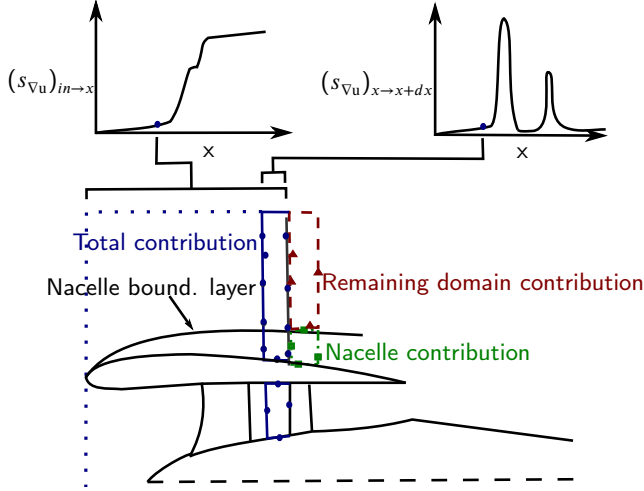


**Figure 26:** Simulation domain discretized in axial subvolumes (dark blue). This subvolume can be split into two subvolumes: the nacelle boundary layer (green) and its complement corresponding to the whole subvolume less the subvolume associated with the nacelle boundary layer (red)

solved part of the TKE production (product of velocity fluctuations) in each cell is known to be more stringent to be accurately computed numerically compared to the two independent variables in the entropy flux method and may also contribute to the discrepancy. In the following, this method based on a local integration in each cell is used since the analysis can be made at a local scale and is adapted to study the losses in restricted control volume like boundary layers.

Based on the boundary layer edge detection method introduced in previous Sec. 5, the boundary layer thickness can be obtained for the different wetted surfaces of the domain (hub, shroud, nacelle, fan, OGV) and the corresponding volumes  $\mathcal{V}_{\text{hub}}$ ,  $\mathcal{V}_{\text{shroud}}$ ,  $\mathcal{V}_{\text{nacelle}}$ ,  $\mathcal{V}_{\text{fan}}$ ,  $\mathcal{V}_{\text{OGV}}$ . The full simulation domain less the boundary layer contributions provides the remaining domain with an associated volume  $\mathcal{V}_{\text{rem. term}}$ . The entropy terms are integrated on these restricted domains to obtain the contributions of the different boundary layers and the remaining domain in a similar manner to previous studies of the losses in gas turbines [10, 11, 17, 24] (see Fig. 26 bottom). The different figures related to the contributions of the boundary layers and the remaining domain are given in conjunction with the total contribution of the domain at the same abscissa to give the reader the magnitude of the contribution to the total one. Similarly to previous Sec. 5, the losses are first analyzed for one OGV geometry (LN) at the three different operating points (AP, CB and SL) then the influence of the OGV geometry on losses is described. In addition, to turn the entropy generation rate integrated over the considered domain into an entropy loss coefficient, the integrated entropy generation rate is divided by the mass flow rate and by a reference dynamic head at the station 1 downstream of the fan for the different operating points based on the mean

velocity magnitude over this plane:

$$\zeta(s) = \frac{T \iiint_{\mathcal{V}} s d\mathcal{V}}{\frac{1}{2} \dot{m}_1 (u_{x,1}^2 + u_{r,1}^2 + u_{\theta,1}^2)} \quad (9)$$

where  $s$  can be the total contribution  $s_{\nabla u}$ , the mean strains contribution  $s_{\nabla u, \text{mean}}$  or the TKE production  $\mathcal{R}_k$  integrated between the inlet of a domain and a position  $x$  (in  $\rightarrow x$ ) or around a position  $x$  ( $x \rightarrow x+dx$ ), the domain  $\mathcal{V}$  being the full domain or restricted domains (boundary layers, remaining domain).

Figure. 27 shows the evolution of the entropy loss coefficient from the inlet to a position  $x$   $\zeta((s_{\nabla u})_{\text{in} \rightarrow x})$ , the contribution due to mean strains dissipation  $\zeta((s_{\nabla u, \text{mean}})_{\text{in} \rightarrow x})$  and TKE production  $\zeta((\mathcal{R}_k)_{\text{in} \rightarrow x})$  along the simulation domain based on the different contributions for the AP operating point. The entropy generation rate starts to increase at the abscissa of the external nacelle and shroud ( $x/D = -0.6$ ) and all the losses are associated to the boundary layer developing over these two surfaces. The contribution of the hub starts to increase at the location of the spinner ( $x/D = -0.29$ ). These two boundary layer contributions increase almost linearly along the simulation domain and are predominantly related to mean strain dissipation until the separation bubble occurring over the shroud surface. At this position the TKE production starts to increase corresponding to the transition and development of a turbulent boundary layer over the shroud boundary layer upstream of the fan leading edge. The region of sharp increase of entropy generation rate corresponds to the fan stage and with a lower magnitude to the OGVs. Similarly to the other wetted surfaces, a boundary layer develops around the PS and SS of these two rows and induces a strong increase in entropy generation rate at the location of the fan between  $x/D = -0.05$  and  $0.07$  and between  $x/D = 0.33$  and  $0.48$  for the OGV. For the fan, the TKE production is dominant compared to the dissipation due to mean strains. For the OGV, the losses are balanced between dissipation due to mean strains and TKE production. When these different contributions are subtracted from the total contribution, the losses referred to as remaining domain containing the tip gap flow, secondary flows, wake and shock losses at CB and SL are isolated. This contribution starts to increase along the fan, in the wake and with a lower magnitude downstream along the OGV. The corresponding losses are mainly related to TKE production.

The different contributions can be integrated over the domain (value at the end of the domain in Fig. 27) to obtain the relative influence on the total amount of losses. The different contributions for the different operating points are gathered in Tab. 4. The table provides the entropy loss coefficient associated to the total entropy generation rate, the dissipation due to mean strains and TKE production. The dissipation due to mean strains represents 45.6% of the total losses at AP and the TKE production is the dominant source of losses with 54.4% of the total losses. This balance between dissipation due to mean strains and TKE production is relatively constant at CB and SL.



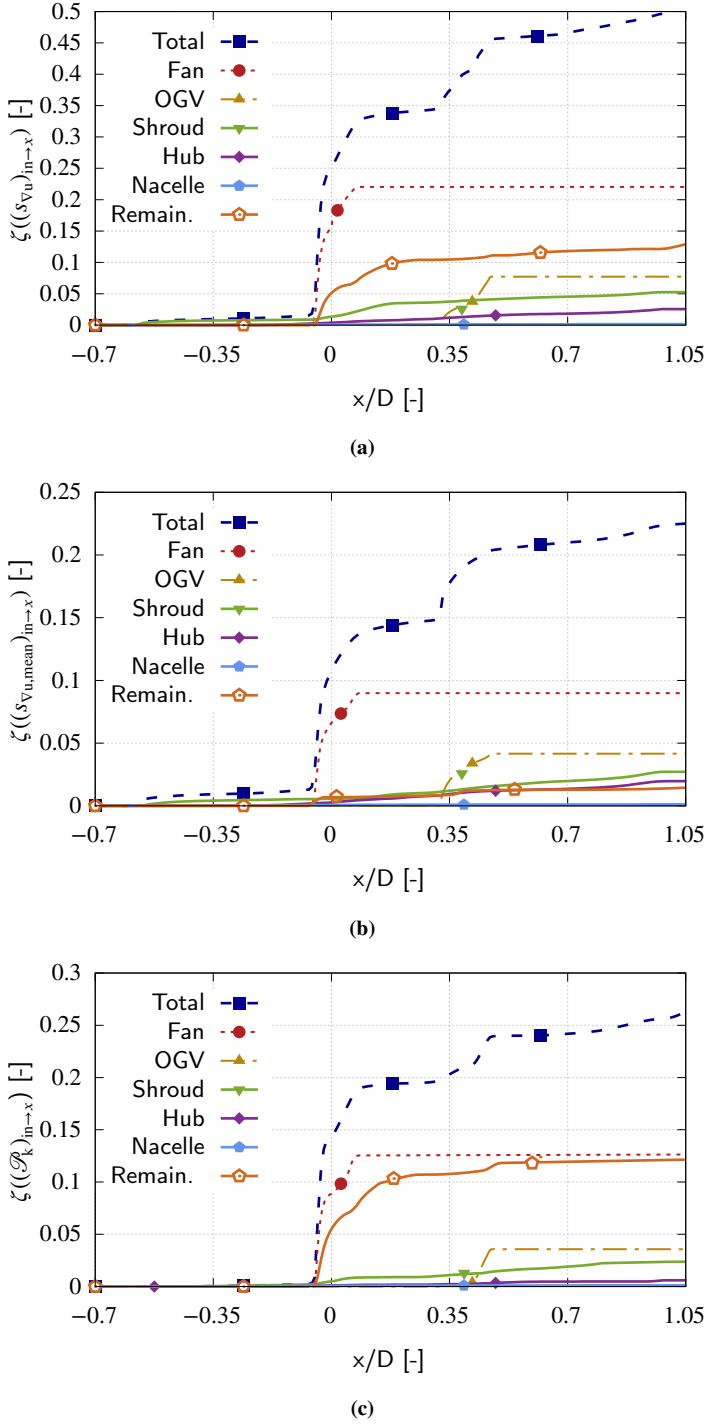


**Figure 27:** Entropy loss coefficient: total  $\zeta((s_{v_u})_{in→x})$  (a), mean strain  $\zeta((s_{v_u,mean})_{in→x})$  (b) and TKE production  $\zeta((\mathcal{P}_k)_{in→x})$  (c) for the AP operating point and LN configuration based on the different contributions

For the AP operating point, the hub boundary layer represents 5.2% of the total losses generated and is less than the shroud boundary contribution (10.3%). This corresponds to the lower extent of the hub surface compared to the shroud with a thinner boundary layer and as a consequence a lower influence in the loss generation. The nacelle boundary layer

contributes to 1.0% of the total losses. Despite a similar wetted surface compared to the shroud, the velocity at the edge of the boundary layer is considerably higher for the shroud (accelerated in-duct flow) compared to the external nacelle where the edge velocity is close to the freestream velocity at  $Ma = 0.1$ . The dominant source of loss is the fan boundary layer with 42.0% of the total losses generated. 84% of this contribution is generated on the SS (35% of the total loss) and 16% on the PS (7% of the total loss). The fan SS boundary layer contributes a lot of loss compared to the PS because of the shock at CB and SL and the adverse pressure gradient inducing a thicker boundary layer. The OGV boundary layer represents 15.9% of the total losses with 80% due to the SS and 20% to the PS. The remaining domain is a strong contributor to losses with 25.9% of the losses. This contribution starts to increase very close to the fan LE ( $x/D = -0.05$ ) and can be related to the LE SS separation bubble that generates strong vortices dissipated within the inter-blade passage and generates losses. This contribution also increases at the fan TE ( $x/D = 0.07$ ) due to the hub passage vortex, tip vortex and wake structures dissipated in the channel.

The hub and shroud boundary layer relative contributions increase with the rotational speed with 5.4% for the hub and 10.8% of the total losses for the shroud at SL. The relative contribution of the nacelle boundary layer decreases with the increasing rotational speed (0.4% of the total losses at CB and 0.3% of losses at SL, respectively). The relative contribution of the fan boundary layer marginally decreases with the increasing rotational velocity, respectively at 41.9% at CB and 40.3% at SL. The relative contribution of the OGV increases with the rotational speed. The relative contribution of the remaining domain is rather constant at higher rotational speed with 26.9% at CB and SL compared to the 25.8% of relative contribution to losses at AP.

The shock structures induce additional losses in the remaining domain at CB and SL since entropy increases when crossing the shock. In the theoretical formulation, shocks are discontinuity with a corresponding thickness of negligible length, in the order of magnitude of a mean free path. Numerically speaking, with finite volume computations, the flow quantity in the simulation domain are continuous. As a consequence, the surface of the shock is indeed enclosing a finite size volume. The corresponding volume is obtained based on a physical shock criterion introduced by Lovely and Haines [25] to determine whether a given cell should be considered as being enclosed by the shock surface:

$$\Psi = \frac{u_i \cdot \frac{\partial p}{\partial x_i}}{c \left( \sum_i \left| \frac{\partial p}{\partial x_i} \right| \right)} \quad (10)$$

where  $c$  is the local speed of sound. If  $\Psi \geq 0.95$  the cell is considered as being enclosed by the wave volume. The corresponding tagged cells for the CB and SL operating points are shown in Fig. 28. The integration of the entropy generation rate on these shock wave volumes represent a contribution of around 1.4% of the remaining domain contribution at

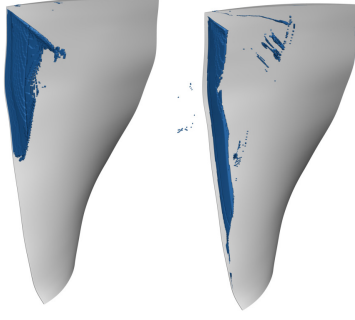


**Figure 28:** Tagged cells ( $\Psi \geq 0.95$ ) defining the shock wave volume at CB (left) and SL (right)

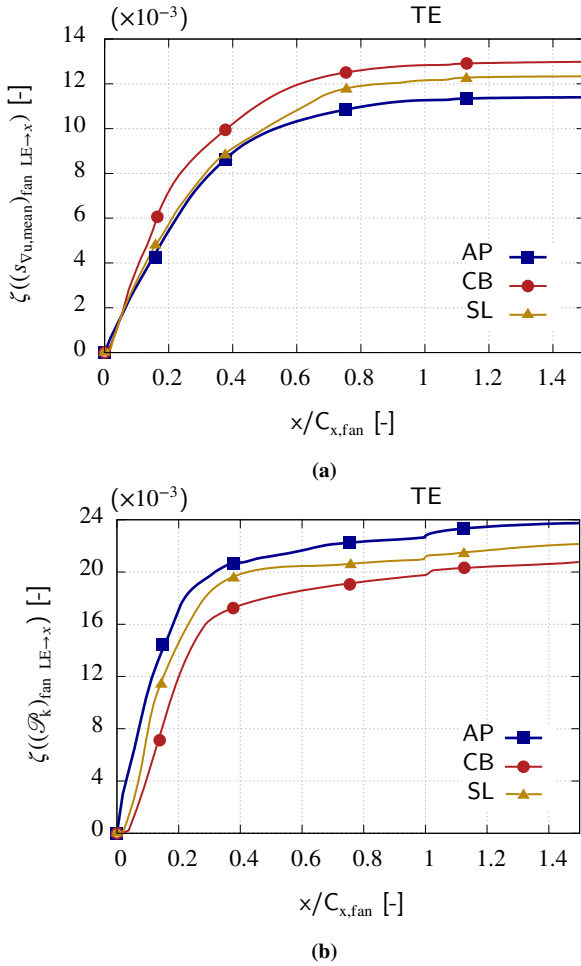


**Figure 29:** Entropy loss coefficient due to mean strains dissipation  $\zeta((s_{\nabla u, \text{mean}})_{\text{fan LE} \rightarrow x})$  (a) and TKE production  $\zeta((P_k)_{\text{fan LE} \rightarrow x})$  (b) integrated from the fan LE in the tip gap for the different operating points

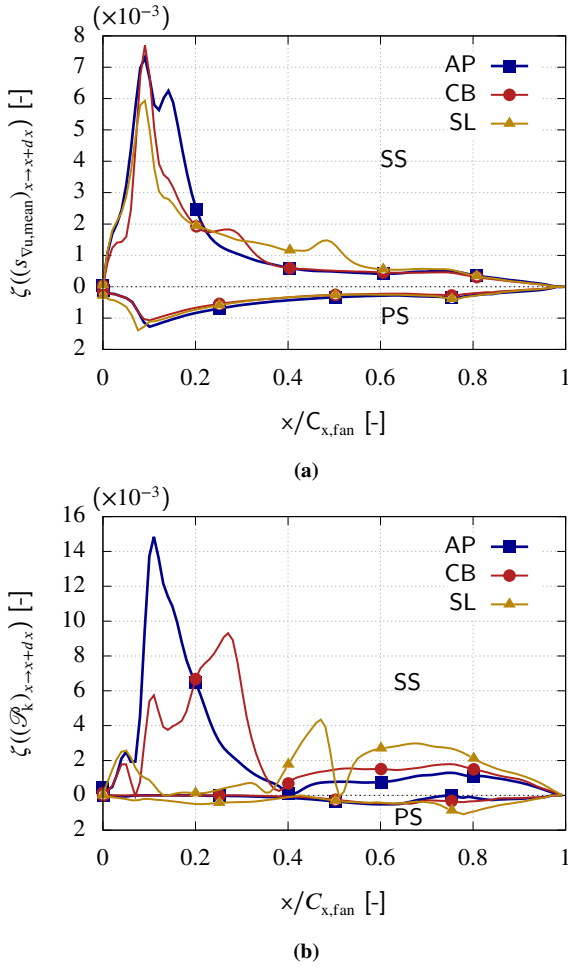
CB and 1.7% at SL. Due to an incident Ma marginally higher than 1 at CB and SL (see Fig. 17) and restricted to the upper part of the blade, the losses associated to the shock wave are relatively weak compared to the total loss generated.

In order to isolate the losses associated with the tip gap flow above the fan blade, the upper part of the remaining domain has been conserved at a radius between 97% and

100% of the channel height and between the LE of the fan blade and 50% axial fan chord downstream of the fan TE. The radial extent considered is higher than the tip gap corresponding to 0.25% of the channel height but makes possible to account for the tip vortex moving radially in the passage. Figure 29 shows the entropy loss coefficient associated to the mean strain dissipation and TKE production in the tip gap integrated from the fan LE for the different operating points. The mean strain dissipation in the tip gap mainly occurs between  $x/C_{x,fan} = 0$  and 0.6. Downstream of the fan TE, the losses associated to mean strains becomes low. For the losses associated to TKE production in the tip gap, two main trends can be identified: between  $x/C_{x,fan} = 0$  and 0.4, the TKE production sharply increases and a second region between  $x/C_{x,fan} = 0.4$  and 1.5 where the TKE production grows less rapidly but keeps increasing downstream of the TE differently from the losses associated to the mean strain dissipation. This trend is observed for the different operating points. In the tip gap, the losses are mainly induced by TKE production (2/3) compared to mean strain dissipation (1/3). The losses associated to the tip gap corresponds to 20-25% of the losses generated in the remaining domain and 6-7% of the total losses generated in the configuration depending on the operating point (see Tab. 4).

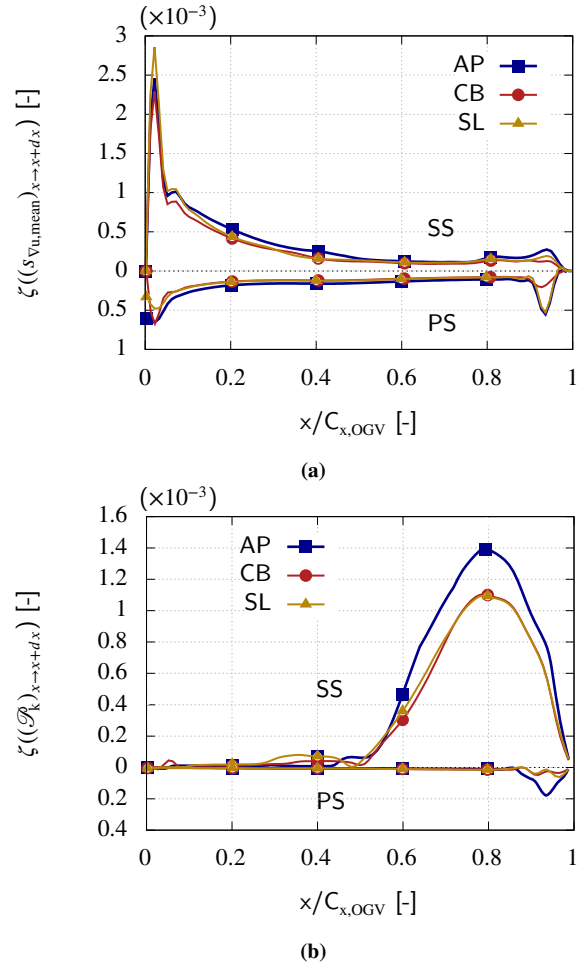
The entropy loss coefficient obtained by integration of the entropy generation rate around the position  $x$  of axial length  $dx$  on the fan SS and PS at AP, CB and SL with the splitting between the dissipation due to the mean strains  $\zeta((s_{\nabla u, \text{mean}})_{x \rightarrow x+dx})$  and TKE production  $\zeta((P_k)_{x \rightarrow x+dx})$  are shown in Fig. 30. For each axial position, the integration of the losses is performed along the whole span. On the SS, the dissipation due to mean strains is mainly produced close to the LE where the flow accelerates and experiences the separation bubble. This contribution constantly decreases up to the TE. On the PS, similarly to the SS, the dissipation due to mean strains is mainly produced close to the LE with a lower magnitude (see Fig. 30a). At AP, the TKE production mainly occurs in a region downstream of the LE separation bubble before to decrease. This contribution increases again from 40%  $C_{x,fan}$  to the TE characterizing the development of the turbulent boundary layer downstream of the enclosed separation bubble. At higher rotational speed (CB and SL), the LE shock progressively shifts the enclosed separation and the turbulent activity is delayed. In particular, the TKE production on the SS is of lower magnitude at SL compared to CB because the transition to turbulence of the boundary layer characterized by the main peak is initiated later at SL ( $x/C_x = 0.5$ ) compared to CB ( $x/C_x = 0.3$ , see Fig. 30b). As a consequence, the decrease of the losses associated to the fan at higher rotational speed (CB and SL) is mainly related to a decrease of the TKE production on the SS.

Figure 31 shows the entropy loss coefficient associated to the dissipation due to mean strains and TKE production integrated around a position  $x$  over the LN OGV SS and PS for the different operating points. For the OGV SS, the dissipation due to mean strains  $s_{\nabla u, \text{mean}}$  is mainly produced close to the LE where the flow accelerates similarly to the



**Figure 30:** Entropy loss coefficient due to mean strains dissipation  $\zeta((s_{\nabla u, \text{mean}})_{x \rightarrow x+dx})$  (a) and TKE production  $\zeta((\mathcal{P}_k)_{x \rightarrow x+dx})$  (b) on the fan SS and PS for the different operating points (integration along the span for each axial position)

fan blade, the production rate then continuously decreases up to the TE. At higher rotational speed (CB and SL), a similar distribution for the dissipation due to mean strains can be observed. On the PS, the dissipation due to mean strains is mainly produced close to the LE with a lower amplitude compared to the SS. On the OGV SS, the TKE production starts to increase downstream of the enclosed recirculation zone where the boundary layer reattaches and becomes turbulent at around  $x/C_{x,\text{OGV}} = 0.5$ . This contribution starts to increase at mid-chord, reaches a maximum value at  $x/C_{x,\text{OGV}} = 0.8$  and decreases to become negligible at the TE. Indeed, the turbulent boundary layer doesn't stop producing turbulence near the TE, the boundary layer separates slightly upstream of the TE and the boundary layer detection method predict a very thin boundary layer in this region close to the TE (see Fig. 24). The main consequence is the TKE production related to that shear layer is transferred to the remaining domain contribution. When the rotational speed is increased, since the boundary layer becomes turbulent slightly upstream on the SS, the level of  $P_k$  increases earlier but with a maximum reached at around  $x/C_{x,\text{OGV}} = 0.8$ .



**Figure 31:** Entropy loss coefficient due to mean strains dissipation  $\zeta((s_{\nabla u, \text{mean}})_{x \rightarrow x+dx})$  (a) and TKE production  $\zeta((\mathcal{P}_k)_{x \rightarrow x+dx})$  (b) on the LN OGV SS and PS at the different operating points (integration along the span for each axial position)

On the PS, the TKE production is almost zero since the boundary layer remains laminar except very close to the TE where local separation and TE wake effects marginally induce TKE production (see Fig. 31b).

The analysis was devoted to the study of losses for a fixed OGV geometry (LN) at the different operating points. The study is now devoted to the analysis of the different OGV geometries to see how different OGV designs can alter loss for different operating conditions. The analysis is first devoted to the losses generated in the OGV boundary layers on the SS and PS. Figure 32 shows the entropy loss coefficient due to mean strains dissipation and TKE production integrated around a position  $x$  of axial length  $dx$  for the different OGV configurations (LC, LN, BA) at CB. The dissipation due to mean strains for the LC and BA OGV geometries display the same trend compared to the LN OGV geometry with large mean strains dissipation occurring close to the LE. The related losses are marginally higher close to the LE for the BA OGV geometry. The TKE production for the BA OGV geometry is initiated earlier compared to the LC and LN OGV geometries since the separation bubble and reat-

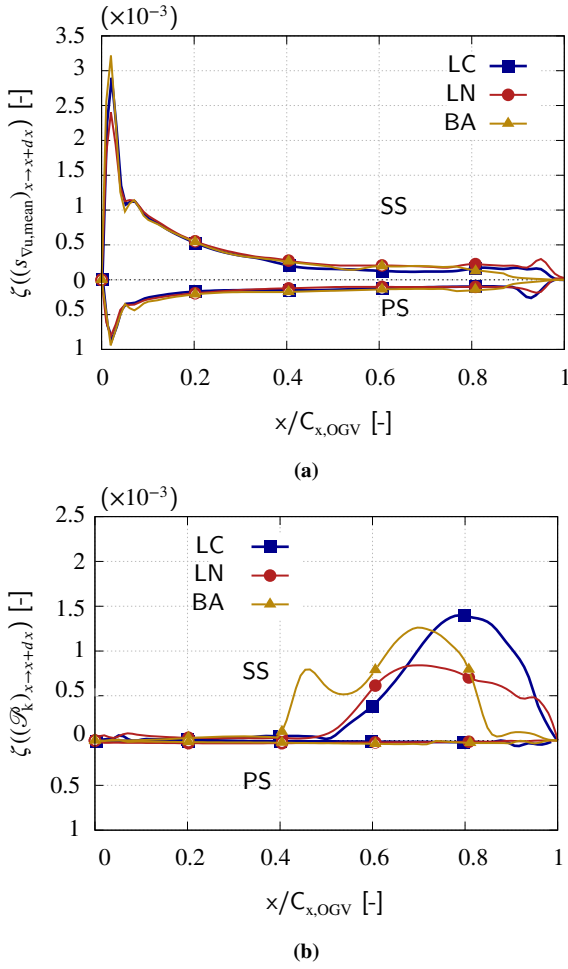


**Figure 32:** Entropy loss coefficient due to mean strains dissipation  $\zeta((s_{V_u,mean})_{x \rightarrow x+dx})$  (a) and TKE production  $\zeta((\mathcal{P}_k)_{x \rightarrow x+dx})$  (b) for the different OGV configurations (LC, LN, BA) at CB (integration along the span for each axial position)

tachment were observed to occur earlier on the blade for the BA geometry. Despite the three OGV geometries were designed to conserve the total aerodynamic losses (the higher chord length of the LC and LN OGV geometries compared to the BA OGV geometry was compensated by a higher number of blades for the BA OGV (54) compared to the LC and LN OGVs (26)), the adverse pressure gradient on the SS may be stronger on the BA OGV geometry promoting this early separation and TKE production.

In order to investigate the influence of the OGV geometry on the losses associated to the remaining domain, the entropy loss coefficient corresponding to the mean strains dissipation and TKE production integrated from the OGV LE to 50% axial chord downstream of the OGV TE for the different OGV geometries at CB is shown in Fig. 33. For the dissipation due to mean strains, the losses increase linearly until 80% of the OGV axial chord and increase more sharply until the OGV TE. Along the OGV, these losses can be related to the hub and shroud passage vortices corresponding to the main vortical structures mixing out gradually in the passage. For the losses associated to the TKE production,

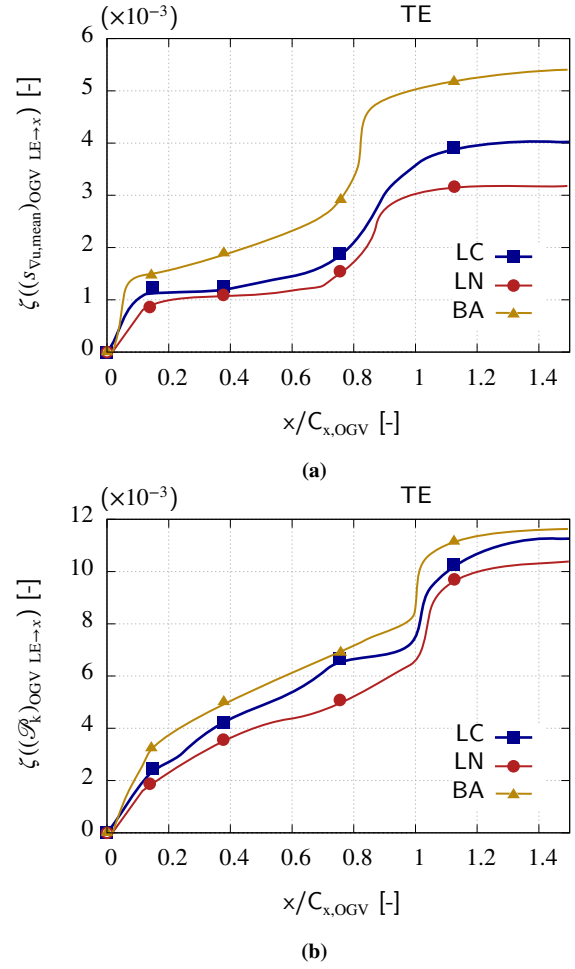


**Figure 33:** Entropy loss coefficient due to mean strains dissipation  $\zeta((s_{V_u,mean})_{OGV LE \rightarrow x})$  (a) and TKE production  $\zeta((\mathcal{P}_k)_{OGV LE \rightarrow x})$  (b) integrated from the OGV LE in the remaining domain for the different OGV configurations (LC, LN, BA) at CB (integration along the span for each axial position)

the losses increase linearly along the OGV and a sudden increase occurs close to the TE associated to the vortex shedding process. The results indicate that the BA OGV induces more dissipation due to mean strains and TKE production compared to the LC and LN geometries. Despite the aerodynamic loading is spread over a higher number of blades, the shorter azimuthal pitch of the BA OGV geometry compared to the LC and LN geometries may promote a higher blade-to-blade azimuthal pressure gradient providing more energy to the hub and shroud passage vortices. Between the LC and LN OGV, the sweeping of the LN OGV compared to the LC OGV reduces the influence of the fan wake at shroud due to the larger axial gap and alter the development of the shroud passage vortex reducing the losses generated.

## 7. Conclusion

The numerical simulation of the NASA SDT for the three different operating points corresponding to approach, cut-back and sideline and the three OGV geometries (baseline,

low-count and low-noise) has been performed based on LES with phase-lagged assumption and POD data storage approach. The simulations showed a good matching with the experimental data: the performance quantities showed a maximum discrepancy of around 1% and 5% for the velocity profiles downstream of the fan.

At approach, the fan is characterized by a leading edge separation bubble over the full span generating wide vortices. Downstream of the recirculation zone, the boundary layer reattaches and becomes turbulent. At cutback and sideline, a leading edge shock followed by an expansion process partially cancel the recirculation zone on the upper part of the blade.

The analysis of the losses based on an entropy approach shows that the hub and shroud boundary layers contribute between 10 and 20% to the total loss generated depending on the operating point. The fan boundary layer contributes between 30 and 40% of total losses and between 10 and 15% for the OGVs. On the fan blade, the dissipation due to mean strains is mainly performed close to the leading edge on the suction side. The turbulent kinetic energy production mainly occurs in the region of the recirculation zone and downstream where the turbulent boundary layer develops. At approach, larger losses are induced on the suction side compared to the cutback and sideline operating points due to a larger turbulent kinetic energy production. At cutback and sideline, the losses associated to the shock waves are relatively weak since the incident Mach number is only marginally higher than unity.

## Acknowledgments

The authors wish to acknowledge Edmane Envia from NASA Glenn Research Center for providing the geometry and experimental data of the NASA SDT, Airbus for technical support, the European commission for having funded this research project within the project SCONE (Grant number 755543) and to ONERA for licensing Cerfacs to use the code elsA. Numerical post-processing has been performed using the python-based library Antares. Part of this work was performed using HPC resources from GENCI-[CCRT-CINES-IDRIS] (Grant 2020-[A0062A06074]).

## A. Derivation of the viscous irreversibility

Following Gibbs' equation for a 3-D non stationary flow, the entropy variation ( $d(\rho s)/dt$ ) experienced by a fluid particle without heat source in the volume can be expressed as:

$$T \frac{d(\rho s)}{dt} = \tau_{ij} \frac{\partial u_i}{\partial x_j} - \frac{\partial q_i}{\partial x_i} \quad (11)$$

where  $q$  is the heat flux. The analysis of the losses in the NASA SDT is here based on mean entropy flux variations using long time averaged quantities. In addition, the thermal contribution to entropy generation is expected to be low compared to the viscous dissipation since the walls are treated

as adiabatic and no large temperature inhomogeneities occur in the flow. Following a statistical averaging approach, the balance equation for the viscous contribution to the entropy balance can be formulated as follows:

$$\left\langle \tau_{ij} \frac{\partial u_i}{\partial x_j} \right\rangle = [\tau_{ij}] \frac{\partial [u_i]}{\partial x_j} + \left\langle \tilde{\tau}_{ij} \frac{\partial u'_i}{\partial x_j} \right\rangle. \quad (12)$$

In LES, the Reynolds stress tensor of the first term in the right hand side of Eq.(12) contains the resolved and sub-grid scale contributions:

$$[\tau_{ij}] = [\tilde{\tau}_{ij} + \mathcal{T}_{ij}] \quad (13)$$

The resolved viscous stress tensor  $[\tilde{\tau}_{ij}]$  corresponds to:

$$[\tilde{\tau}_{ij}] = \mu \left( \frac{\partial [u_i]}{\partial x_j} + \frac{\partial [u_j]}{\partial x_i} \right) \quad (14)$$

The sub-grid Reynolds stress tensor  $[\mathcal{T}_{ij}] = [\bar{\rho} \tilde{u}_i \tilde{u}_j - \overline{\rho u_i u_j}]$  is modeled using a Boussinesq assumption:

$$[\mathcal{T}_{ij}] = \mu_{SGS} \left( \frac{\partial [u_i]}{\partial x_j} + \frac{\partial [u_j]}{\partial x_i} \right). \quad (15)$$

The dissipation due to mean strains can be then written as:

$$[\tau_{ij}] \frac{\partial [u_i]}{\partial x_j} = (\mu + \mu_{SGS}) \left( \frac{\partial [u_i]}{\partial x_j} + \frac{\partial [u_j]}{\partial x_i} \right) \frac{\partial [u_i]}{\partial x_j}. \quad (16)$$

The second term in the right hand side of Eq.(12) can be obtained based on the equation for the budget of the turbulent kinetic energy in compressible LES  $k = \langle \bar{\rho} u_i'^2 / 2 \rangle$  [3]:

$$\begin{aligned} 0 = & \underbrace{-\frac{\partial}{\partial x_j} \left( \frac{1}{2} \langle \bar{\rho} u_i'^2 \rangle [u_j] \right)}_{\text{Mean flow convection}} - \underbrace{\langle \bar{\rho} u'_i u'_j \rangle \frac{\partial [u_i]}{\partial x_j}}_{\text{Production}} - \underbrace{\frac{1}{2} \frac{\partial}{\partial x_j} \langle \bar{\rho} u_i'^2 u'_j \rangle}_{\text{Turbulence diffusion}} \\ & - \underbrace{\left\langle \tilde{\tau}_{ij} \frac{\partial u'_i}{\partial x_j} \right\rangle}_{\text{dissipation}} - \underbrace{\left\langle \mathcal{T}_{ij} \frac{\partial u'_i}{\partial x_j} \right\rangle}_{\text{dissipation}} + \frac{\partial}{\partial x_{ij}} \langle u'_i \tilde{\tau}_{ij} \rangle + \frac{\partial}{\partial x_i} \langle u'_i \mathcal{T}_{ij} \rangle \\ & - \underbrace{\frac{\partial}{\partial x_i} \langle p' u'_i \rangle}_{\text{Pressure diffusion}} + \underbrace{\left\langle p' \frac{\partial u'_i}{\partial x_i} \right\rangle}_{\text{Pressure-dilatation term}} - \langle u'_i \rangle \frac{\partial \langle \bar{p} \rangle}{\partial x_i} \end{aligned} \quad (17)$$

the main terms in the energy equation being underlined. The diffusive-like terms in Eq.(17) cannot generate or consume TKE, they just redistribute it. The dissipation term can be then written as:

$$\left\langle \tilde{\tau}_{ij} \frac{\partial u'_i}{\partial x_j} \right\rangle = - \langle \bar{\rho} u'_i u'_j \rangle \frac{\partial [u_i]}{\partial x_j} - \left\langle \mathcal{T}_{ij} \frac{\partial u'_i}{\partial x_j} \right\rangle. \quad (18)$$

The first term on the right hand side corresponds to resolved the part of the turbulence production. The second term on the right hand side of Eq.(18) corresponds to the modelled Reynolds stresses that makes possible to account for the unresolved part of the turbulence production.

**Table 4**

Repartition of losses (entropy loss coefficient  $\zeta$ ) for the different operating points based on the LN configuration (relative contribution to total losses between parenthesis)

Contribution	AP	CB	SL
$\zeta$	Total		
$(s_{Vu})_{in \rightarrow out}$	0.535 (100%)	0.501 (100%)	0.464 (100%)
$(s_{Vu,m.})_{in \rightarrow out}$	0.244 (45.6%)	0.230 (45.9%)	0.215 (46.4%)
$(\mathcal{R}_k)_{in \rightarrow out}$	0.291 (54.4%)	0.271 (54.1%)	0.249 (53.6%)
Fan			
$(s_{Vu})_{in \rightarrow out}$	0.225 (42.0%)	0.210 (41.9%)	0.187 (40.3%)
$(s_{Vu,m.})_{in \rightarrow out}$	0.093 (17.3%)	0.090 (17.9%)	0.090 (19.4%)
$(\mathcal{R}_k)_{in \rightarrow out}$	0.132 (24.7%)	0.120 (24.0%)	0.097 (20.9%)
Fan SS			
$(s_{Vu})_{in \rightarrow out}$	0.187 (35.0%)	0.172 (34.3%)	0.140 (30.1%)
$(s_{Vu,m.})_{in \rightarrow out}$	0.068 (12.7%)	0.065 (13.0%)	0.060 (12.9%)
$(\mathcal{R}_k)_{in \rightarrow out}$	0.119 (22.3%)	0.107 (21.3%)	0.080 (17.2%)
Fan PS			
$(s_{Vu})_{in \rightarrow out}$	0.038 (7.0%)	0.038 (7.4%)	0.047 (10.1%)
$(s_{Vu,m.})_{in \rightarrow out}$	0.025 (4.6%)	0.025 (5.0%)	0.030 (6.5%)
$(\mathcal{R}_k)_{in \rightarrow out}$	0.013 (2.4%)	0.013 (2.4%)	0.017 (3.6%)
OGV			
$(s_{Vu})_{in \rightarrow out}$	0.085 (15.9%)	0.081 (16.2%)	0.076 (16.4%)
$(s_{Vu,m.})_{in \rightarrow out}$	0.046 (8.6%)	0.046 (9.2%)	0.044 (9.5%)
$(\mathcal{R}_k)_{in \rightarrow out}$	0.039 (7.3%)	0.035 (7.0%)	0.032 (6.9%)
OGV SS			
$(s_{Vu})_{in \rightarrow out}$	0.068 (12.7%)	0.067 (13.3%)	0.062 (13.4%)
$(s_{Vu,m.})_{in \rightarrow out}$	0.031 (5.8%)	0.033 (6.7%)	0.031 (6.7%)
$(\mathcal{R}_k)_{in \rightarrow out}$	0.037 (6.9%)	0.034 (6.8%)	0.031 (6.7%)
OGV PS			
$(s_{Vu})_{in \rightarrow out}$	0.017 (3.2%)	0.014 (2.9%)	0.014 (3.0%)
$(s_{Vu,m.})_{in \rightarrow out}$	0.015 (2.8%)	0.013 (2.6%)	0.013 (2.8%)
$(\mathcal{R}_k)_{in \rightarrow out}$	0.002 (0.4%)	0.001 (0.2%)	0.001 (0.2%)
Shroud			
$(s_{Vu})_{in \rightarrow out}$	0.055 (10.3%)	0.043 (8.7%)	0.050 (10.8%)
$(s_{Vu,m.})_{in \rightarrow out}$	0.024 (4.5%)	0.019 (3.8%)	0.021 (4.5%)
$(\mathcal{R}_k)_{in \rightarrow out}$	0.031 (5.8%)	0.024 (4.8%)	0.029 (6.3%)
Hub			
$(s_{Vu})_{in \rightarrow out}$	0.028 (5.2%)	0.026 (5.2%)	0.025 (5.4%)
$(s_{Vu,m.})_{in \rightarrow out}$	0.021 (3.9%)	0.018 (3.6%)	0.020 (4.3%)
$(\mathcal{R}_k)_{in \rightarrow out}$	0.007 (1.3%)	0.008 (1.6%)	0.005 (1.1%)
Nacelle			
$(s_{Vu})_{in \rightarrow out}$	0.005 (1.0%)	0.002 (0.4%)	0.0015 (0.3%)
$(s_{Vu,m.})_{in \rightarrow out}$	0.004 (0.7%)	0.0015 (0.3%)	0.0012 (0.2%)
$(\mathcal{R}_k)_{in \rightarrow out}$	0.001 (0.3%)	0.0005 (0.1%)	0.0003 (0.1%)
Remaining domain			
$(s_{Vu})_{in \rightarrow out}$	0.137 (25.8%)	0.135 (26.9%)	0.125 (26.9%)
$(s_{Vu,m.})_{in \rightarrow out}$	0.025 (6.7%)	0.051 (10.3%)	0.039 (8.4%)
$(\mathcal{R}_k)_{in \rightarrow out}$	0.112 (18.9%)	0.084 (16.7%)	0.086 (18.5%)
Tip gap flow			
$(s_{Vu})_{in \rightarrow out}$	0.0352 (6.6%)	0.0336 (6.7%)	0.0343 (7.4%)
$(s_{Vu,m.})_{in \rightarrow out}$	0.0116 (2.2%)	0.0129 (2.6%)	0.0124 (2.7%)
$(\mathcal{R}_k)_{in \rightarrow out}$	0.0236 (4.4%)	0.0207 (4.1%)	0.0219 (4.7%)

## References

- [1] C. P. Arroyo, T. Leonard, M. Sanjose, S. Moreau, and F. Duchaine. Large eddy simulation of a rotor stage for fan noise source diagnostic. In *Global Power and Propulsion Forum*, pages 7–19, Montreal, QC, Canada, 2018. Zenodo.
- [2] G Berkooz. The Proper Orthogonal Decomposition in the Analysis of Turbulent Flows. *Annual Review of Fluid Mechanics*, 25(1):539–575, 2002. doi: 10.1146/annurev.fluid.25.1.539.
- [3] C. Bogey and C. Bailly. Large eddy simulations of round free jets using explicit filtering with/without dynamic Smagorinsky model. *International Journal of Heat and Fluid Flow*, 27(4):603–610, 2006. ISSN 0142727X. doi: 10.1016/j.ijheatfluidflow.2006.02.008.
- [4] L. Cambier and J.P. Vuillot. Status of the elsA software for flow simulation and multi-disciplinary applications. In *46th AIAA Aerospace Sciences Meeting and Exhibit*, page 664, 2008. doi: 10.2514/6.2008-664.
- [5] L. Cambier, S. Heib, and S. Plot. The Onera elsA CFD software: input from research and feedback from industry. *Mechanics & Industry*, 14(3):159–174, 2013. doi: 10.1051/meca/2013056.
- [6] D. Casalino, A. Hazir, and A. Mann. Turbofan Broadband Noise Prediction Using the Lattice Boltzmann Method. *AIAA Journal*, 56(2):132–143, 2017. doi: 10.2514/1.j055674.
- [7] J. Cliquet, R. Houdeville, and D. Arnal. Application of Laminar-Turbulent Transition Criteria in Navier-Stokes Computations. *AIAA Journal*, 46(5):1182–1190, 2008. doi: 10.2514/1.30215.
- [8] J. Cousteix. Three-Dimensional and Unsteady Boundary-Layer Computations. *Annual Review of Fluid Mechanics*, 18(2):173–196, 1986. doi: 10.1146/annurev.fluid.18.1.173.
- [9] J. Cui, V. Nagabhushana Rao, and P. G. Tucker. Numerical investigation of secondary flows in a high-lift low pressure turbine. *International Journal of Heat and Fluid Flow*, 63(1):149–157, 2017. doi: 10.1016/j.ijheatfluidflow.2016.05.018.
- [10] J. D. Denton. Loss Mechanisms in Turbomachines. *Journal of Turbomachinery*, 115(4):621, 1993. doi: 10.1115/1.2929299.
- [11] J. D. Denton and G. Pullan. A Numerical Investigation Into the Sources of Endwall Loss in Axial Flow Turbines. In *Volume 8: Turbomachinery, Parts A, B, and C*, page 1417, 2012. doi: 10.1115/GT2012-69173.
- [12] J. Erdos and E. Alzner. Computation of unsteady transonic flows through rotating and stationary cascades. I: Method of analysis. Technical report, National Aeronautics and Space Administration, 1977.
- [13] E. Garnier, N. Adams, and P. Sagaut. *LES for compressible flows*. 2009. ISBN 9789048128181.
- [14] N. Gourdain. Prediction of the unsteady turbulent flow in an axial compressor stage. Part 1: Comparison of unsteady RANS and LES with experiments. *Computers and Fluids*, 2015. doi: 10.1016/j.compfluid.2014.09.052.
- [15] N. Gourdain. Prediction of the unsteady turbulent flow in an axial compressor stage. Part 2: Analysis of unsteady RANS and LES data. *Computers and Fluids*, 2015. doi: 10.1016/j.compfluid.2014.09.044.
- [16] N. Gourdain, F. Sicot, F. Duchaine, and L. Gicquel. Large eddy simulation of flows in industrial compressors: a path from 2015 to 2035. *Phil. Trans. R. Soc. A*, 372(2022):20130323, 2014. doi: 10.1098/rsta.2013.0323.
- [17] F. Hammer, N. Sandham, and R. Sandberg. The Influence of Different Wake Profiles on Losses in a Low Pressure Turbine Cascade. *International Journal of Turbomachinery, Propulsion and Power*, 2018. doi: 10.3390/ijtpp3020010.

- [18] L. He. Method of simulating unsteady turbomachinery flows with multiple perturbations. *AIAA Journal*, 30(11):2730–2735, 1992. doi: 10.2514/3.11291.
- [19] L. He. Fourier methods for turbomachinery applications. *Progress in Aerospace Sciences*, 46(8):329–341, 2010. doi: 10.1016/j.paerosci.2010.04.001.
- [20] L. J. Heidelberg. Fan noise source diagnostic test - Tone modal structure results. In *8th AIAA/CEAS Aeroacoustics Conference and Exhibit*, 2002. doi: 10.2514/6.2002-2428.
- [21] A. Jameson, W. Schmidt, and E. Turkel. Numerical solutions of the Euler equations by finite volume methods using Runge-Kutta time-stepping schemes. *AIAA paper*, 6(2):1259, 1981. doi: 10.2514/6.1981-1259.
- [22] D. Lengani, D. Simoni, M. Ubaldi, P. Zunino, and F. Bertini. A POD-Based Procedure for the Split of Unsteady Losses of an LPT Cascade. *International Journal of Turbomachinery, Propulsion and Power*, 2(4):17, 2017. doi: 10.3390/ijtp2040017.
- [23] D. Lengani, D. Simoni, M. Ubaldi, P. Zunino, F. Bertini, and V. Michelassi. Accurate Estimation of Profile Losses and Analysis of Loss Generation Mechanisms in a Turbine Cascade. *Journal of Turbomachinery*, 139(12):121–132, 2017. doi: 10.1115/1.4037858.
- [24] D. Lengani, D. Simoni, R. Pichler, R. D. Sandberg, V. Michelassi, and F. Bertini. Identification and quantification of losses in a LPT cascade by POD applied to LES data. *International Journal of Heat and Fluid Flow*, 70:28–40, 2018. doi: 10.1016/j.ijheatfluidflow.2018.01.011.
- [25] D. Lovely and R. Haimes. Shock detection from computational fluid dynamics results. In *14th Computational Fluid Dynamics Conference*, 1999. doi: 10.2514/6.1999-3285.
- [26] C. Marmignon, V. Couaillier, and B. Courbet. Solution Strategies for Integration of Semi-Discretized Flow Equations in elsA and CEDRE. *AerospaceLab Journal*, 2(1):1–11, 2011.
- [27] V. Michelassi and J. G. Wissink. Turbulent kinetic energy production in the vane of a low-pressure linear turbine cascade with incoming wakes. *International Journal of Rotating Machinery*, 2015(2), 2015. doi: 10.1155/2015/650783.
- [28] V. Michelassi, F. Martelli, D. J. Dénos, T. Arts, and C. H. Sieverding. Unsteady heat transfer in stator-rotor interaction by two-equation turbulence model. *Journal of Turbomachinery*, 1999. doi: 10.1115/1.2841336.
- [29] G. Mouret, N. Gourdain, and L. Castillon. Adaptation of Phase-Lagged Boundary Conditions to Large Eddy Simulation in Turbomachinery Configurations. *Journal of Turbomachinery*, 138(4):041003, 2015. doi: 10.1115/1.4032044.
- [30] F. Nicoud and F. Ducros. Subgrid-scale stress modelling based on the square of the velocity gradient tensor. *Flow, Turbulence and Combustion*, 62(3):183–200, 1999. doi: 10.1023/A:1009995426001.
- [31] H. Nishikawa, M. Rad, and P. Roe. A third-order fluctuation splitting scheme that preserves potential flow. In *15th AIAA Computational Fluid Dynamics Conference*, 2013. doi: 10.2514/6.2001-2595.
- [32] R. Pichler, Y. Zhao, R. D. Sandberg, V. Michelassi, R. Pacciani, M. Marconcini, and A. Arnone. LES and RANS analysis of the end-wall flow in a linear LPT cascade with variable inlet conditions, Part I: Flow and secondary vorticity fields. In *ASME Turbo Expo 2018: Turbomachinery Technical Conference and Exposition*, Oslo, Norway, 2018. ASME. doi: 10.1115/GT2018-76450.
- [33] U. Piomelli. Wall-layer models for large-eddy simulations. *Progress in Aerospace Sciences*, 44(6):437–446, 2008. doi: 10.1016/j.paerosci.2008.06.001.
- [34] G. G. Podboy, M. J. Krupar, S. M. Helland, and C. E. Hughes. Steady and unsteady flow field measurements within a NASA 22 inch fan model. In *40th AIAA Aerospace Sciences Meeting and Exhibit*, 2002. doi: 10.2514/6.2002-1033.
- [35] G. G. Podboy, M. J. Krupar, C. E. Hughes, and R. P. Woodward. Fan noise source diagnostic test - LDV measured flow field results. In *8th AIAA/CEAS Aeroacoustics Conference and Exhibit*, 2002. doi: 10.2514/6.2002-2431.
- [36] P. Sagaut. *Large Eddy Simulation for Incompressible Flows: An Introduction*. Springer Science & Business Media, 2006. doi: 10.1007/b137536.
- [37] P. Sagaut, S. Deck, and M. Terracol. *Multiscale and Multiresolution Approaches in Turbulence, LES, DES and Hybrid RANS/LES Methods: Applications and Guidelines*. World Scientific, 2013. doi: 10.1142/p878.
- [38] M. Shur, M. Strelets, A. Travin, P. Spalart, and T. Suzuki. Unsteady simulations of a fan/outlet-guide-vane system: Aerodynamics and turbulence. *AIAA Journal*, 2018. doi: 10.2514/1.J056645.
- [39] P. G. Tucker. Computation of unsteady turbomachinery flows: Part 2-LES and hybrids. *Progress in Aerospace Sciences*, 47(7):546–569, 2011. doi: 10.1016/j.paerosci.2011.07.002.
- [40] A. P. S. Wheeler, R.D. Sandberg, N. D. Sandham, R. Pichler, V. Michelassi, and G. Laskowski. Direct Numerical Simulations of a High-Pressure Turbine Vane. *Journal of Turbomachinery*, 138(7):071003, 2016. doi: 10.1115/1.4032435.
- [41] D. C. Wilcox. Formulation of the  $k-\omega$  turbulence model revisited. In *AIAA Journal*, 2008. doi: 10.2514/1.36541.